

# 1 Sparse recurrent excitatory connectivity in the microcircuit 2 of the adult mouse and human cortex

3 Stephanie C. Seeman<sup>1</sup><sup>✉</sup>, Luke Campagnola<sup>1</sup><sup>✉</sup>, Pasha A. Davoudian<sup>1</sup>, Alex Hoggarth<sup>1</sup>, Travis A.  
4 Hage<sup>1</sup>, Alice Bosma-Moody<sup>1</sup>, Christopher A. Baker<sup>1</sup>, Jung Hoon Lee<sup>1</sup>, Stefan Mihalas<sup>1</sup>, Corinne  
5 Teeter<sup>1</sup>, Andrew L. Ko<sup>2,3</sup>, Jeffrey G. Ojemann<sup>2,3</sup>, Ryder P. Gwinn<sup>4</sup>, Daniel L. Silbergeld<sup>3</sup>, Charles  
6 Cobbs<sup>5</sup>, John Phillips<sup>1</sup>, Ed Lein<sup>1</sup>, Gabe J. Murphy<sup>1</sup>, Christof Koch<sup>1</sup>, Hongkui Zeng<sup>1</sup>, Tim Jarsky<sup>1</sup><sup>✉</sup>

7 <sup>✉</sup>These authors contributed equally to this work.

8 <sup>✉</sup>Correspondence should be addressed to T.J. ([timj@alleninstitute.org](mailto:timj@alleninstitute.org))

9 1 Allen Institute for Brain Science, Seattle, WA;

10 2 Regional Epilepsy Center at Harborview Medical Center, Seattle, WA;

11 3 Department of Neurological Surgery, University of Washington School of Medicine, Seattle, WA;

12 4 Epilepsy Surgery and Functional Neurosurgery, Swedish Neuroscience Institute, Seattle, WA;

13 5 The Ben and Catherine Ivy Center for Advanced Brain Tumor Treatment, Swedish Neuroscience  
14 Institute, Seattle, WA

## 15 Abstract

16 Generating a comprehensive description of cortical networks requires a large-scale, systematic  
17 approach. To that end, the Allen Institute is engaged in a pipeline project using multipatch  
18 electrophysiology, supplemented with 2-photon optogenetics, to characterize connectivity and  
19 synaptic signaling between classes of neurons in adult mouse and human cortex. We focus on  
20 producing results detailed enough for the generation of computational models and enabling  
21 comparison with future studies. Here we report our examination of intralaminar connectivity  
22 within each of several classes of excitatory neurons. We find that connections are sparse but  
23 present among all excitatory cell types and layers we sampled, with the most sparse  
24 connections in layers 5 and 6. Almost all mouse synapses exhibited short-term depression with  
25 similar dynamics. Synaptic signaling between a subset of layer 2/3 neurons; however, exhibited  
26 facilitation. These results contribute to a body of evidence describing recurrent excitatory  
27 connectivity as a conserved feature of cortical microcircuits.

## 28 Introduction

29 Generating well-informed, concrete, testable hypotheses about how the cortex represents and  
30 processes information requires experimental efforts to characterize the connectivity and  
31 dynamics of cortical circuit elements as well as efforts to build models that integrate results  
32 across studies (Sejnowski et al. 1988). Estimates of connectivity and synaptic properties vary  
33 widely between experiments due to differences in model organisms, experimental parameters,

34 and analytic methods. This variability limits our ability to generate accurate, integrative  
35 computational models.

36 Addressing this problem requires standardized experimental methods and large-scale data  
37 collection in order to characterize synaptic connections between the large number of potential  
38 cell types (Tasic et al. 2016). Although it may be possible to infer part of these results based  
39 solely on anatomical constraints (Markram et al. 2015), evidence has shown that the rate of  
40 connectivity and properties of synaptic signals can depend on the identity of the pre- and  
41 postsynaptic neuron (Reyes et al. 1998, Galarreta and Hestrin, 1998). To collect standardized  
42 data at scale, the Allen Institute for Brain Science has built a pipeline to characterize local,  
43 functional connectivity in the adult mouse and human cortex. Here we report on the  
44 characteristics of recurrent, intralayer connectivity among pyramidal neurons generated during  
45 the pipeline's system integration test—an end-to-end test of the pipeline's hardware, software,  
46 and workflow for a subset of all synaptic connections.

47 Recurrent excitatory connectivity is a common feature in computational models of cortical  
48 working memory, receptive field shaping, attractor dynamics, and sequence storage (Camperi &  
49 Wang 1998, Olshausen & Field 1996, Brunel et al. 2016, Pernice et al. 2018). Empirical  
50 measurements of recurrent connectivity and synaptic properties are needed in order to  
51 constrain and validate these models. However, characterizing recurrent connectivity in a  
52 standardized, high throughput manner is challenging because the synaptic connections can be  
53 sparse and weak (Braitenberg and Schüz 1998, Lefort 2009). Furthermore, most measurements  
54 of recurrent connectivity have been performed in juvenile rodents, leading to a recent debate  
55 over the rate of connectivity in the adult cortex (Biane et al. 2015, Barth et al. 2016, Jiang et al.  
56 2016).

57 The data reported here demonstrate that sparse recurrent connectivity is present among  
58 excitatory neurons in all layers of adult mouse and human cortex. Using a novel automated  
59 method for systematically estimating connectivity across experiments we further demonstrate  
60 that different populations of adult mouse pyramidal neurons exhibit characteristic distance-  
61 dependent connectivity profiles and short-term dynamics. We quantify and compare differences  
62 in short-term dynamics with a mechanistic computational model.

## 63 Results

64 Here, we report on data collected during the system integration test of a new Allen Institute for  
65 Brain Science pipeline for the systematic characterization of local connectivity in the adult  
66 cortex. We performed *in vitro* whole-cell recordings from up to eight excitatory neurons  
67 simultaneously. To assess connectivity, trains of action potentials were evoked in each cell, one  
68 at a time, while recording current clamp synaptic responses in all other cells. We probed 2324  
69 putative connections (200 minimum per layer) in mouse V1 and 332 putative connections (35  
70 minimum per layer) in human frontal and temporal cortex (Table 1). Connections were identified  
71 by the presence of excitatory PSPs (EPSPs) evoked with a short latency and low jitter, following  
72 the presynaptic spike, consistent with a monosynaptic connection (Figure S1). Recurrent

73 connectivity was observed in layer 2/3 through layer 6 of mouse primary visual cortex and layer  
74 2 through layer 5 of the human cortex.

75 **Table 1: Number of potential connections used in each connection analysis**

Layer / Cell Type	Total Probed (Fig 1C)	Total connected (Fig 1C)	Strength (Fig 1E)	Kinetics (Fig 1F)	Connection Probability (%) w/in 100 $\mu$ m (Connected/probed, Fig 1D)	STP (Fig 1G)
Mouse L2/3	255	20	12	9	17/178 (9.55)	9
Rorb	282	20	13	13	19/205 (9.27)	9
Sim1	524	34	18	18	31/382 (8.12)	7
Tlx3	969	34	17	14	28/661 (4.24)	5
Ntsr1	318	1	1	1	0/223 (0.0)	N/A
Human L2	38	4	4	4	3/24 (12.5)	N/A
Human L3	187	42	33	29	22/90 (24.44)	N/A
Human L4	38	2	1	1	0/35 (0.0)	N/A
Human L5	69	9	6	6	4/33 (12.12)	N/A

76 Properties of intralaminar excitatory synaptic signaling in mouse cortex

77 Layer and projection-specific subclasses of excitatory neuron populations were identified either  
78 by *post-hoc* morphologic evaluation in layer 2/3 or transgenic labelling to target layers 4-6  
79 (Rorb, Tlx3, Sim1, and Ntsr1, respectively; Figure 1A). Layer 5 recordings were subdivided into  
80 subcortical projecting cells (Sim1) or corticocortical projecting cells (Tlx3). We probed 2384  
81 potential connections (layer 2/3: 255, Rorb: 282, Sim1: 524, Tlx3: 969, Ntsr1: 318) across these  
82 excitatory populations in mouse cortex (Table 1). Connections were detected between 107  
83 putative pre- and post-synaptic partners (layer 2/3: 20, Rorb: 20, Sim1: 34, Tlx3: 34, Ntsr1: 1;  
84 Table 1). For >75% of the recorded cells, we recovered a biocytin fill (Fig 1A) and for all cells we  
85 obtained an epifluorescent image stack (Fig 1B).

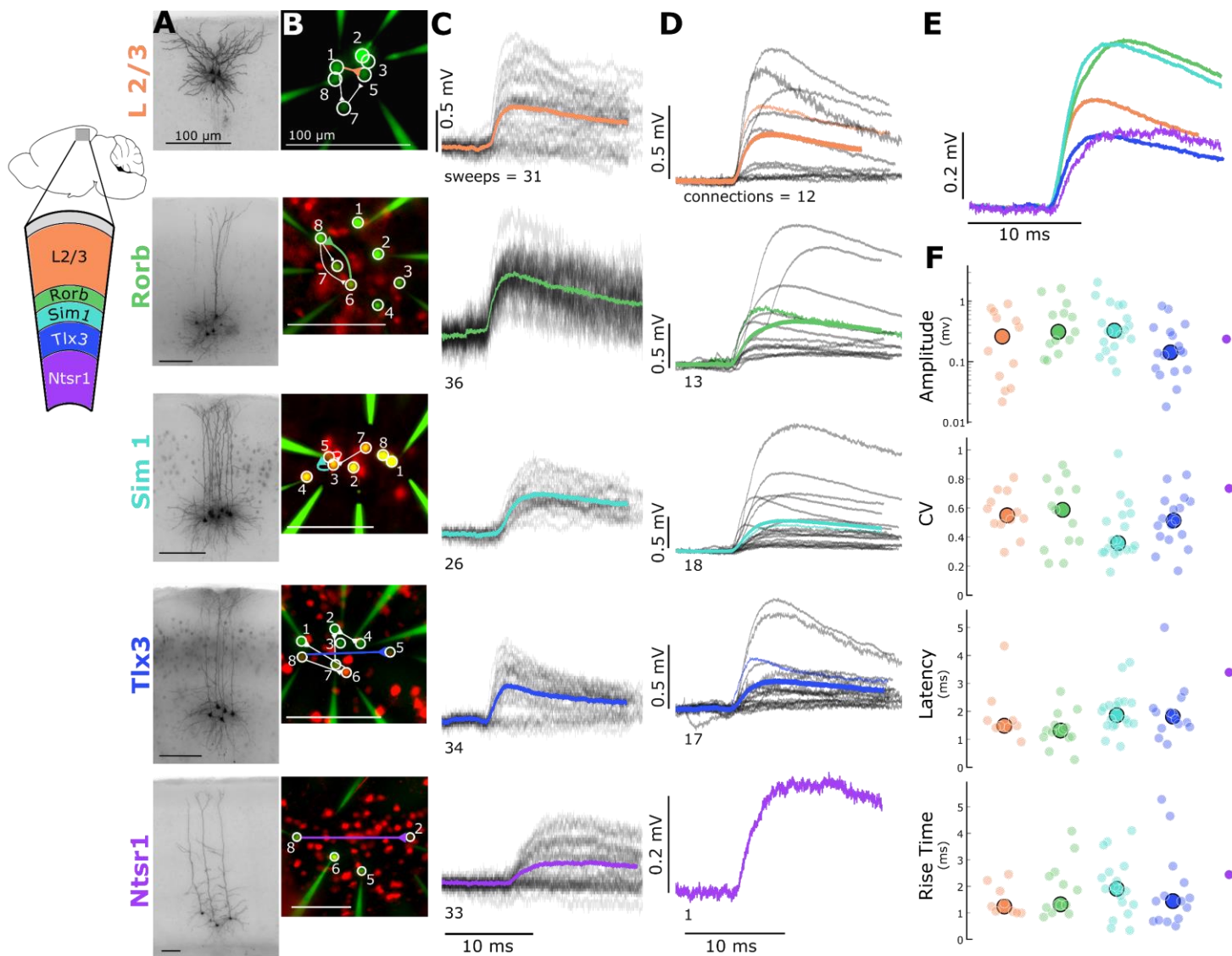


**Figure 1.** Electrophysiological recordings of evoked excitatory synaptic responses between individual cortical pyramidal neurons in mouse primary visual cortex. **A.** Cartoon illustrating color, Cre-type, and cortical layer mapping in slice recording region (V1). Example maximum intensity projection images of biocytin-filled pyramidal neurons for L2/3 and each Cre-type. **B.** Example epifluorescent images of neurons showing Cre-dependent reporter expression and/or dye-filled recording pipettes. Connection map is overlaid on the epifluorescent image (colored: example connection shown in C). **C.** Spike time aligned EPSPs induced by the first AP of all  $\leq 50$  Hz stimulus trains for a single example connection (individual pulse-response trials: grey; average: colored). **D.** First pulse average, like in C., for all connections within the synaptic type; grey: individual connections; thin-colored: connection highlighted in C.; thick-colored: grand average of all connections. **E.** Overlay of grand average for each connection type. **F.** EPSP amplitude (in log units), CV of amplitude, latency, and rise time of first pulse response for each Cre type (small circles) with the grand median (large).

86 In layers 2/3 through 5 we were able to sample sufficiently to characterize the strength and  
 87 kinetics in recurrent connections. To measure these features with minimal influence of STP,  
 88 only the first response on each sweep (ITI = 15s) was included for this analysis. A subset of  
 89 connections from each group were chosen based on quality control metrics and inclusion  
 90 criteria (see methods; Fig S1). Figure 1C shows EPSPs recorded from one example connection  
 91 found in each of the five chosen excitatory cell groups. For the large majority of connections, it

92 was not possible to unequivocally distinguish synaptic failures from detection failures, thus we  
93 used the mean response from all sweeps (Fig 1C) to evaluate the EPSP features.

94 Consistent with previous reports that recurrent connectivity is weak (Lefort 2009), we found that  
95 a majority of the connections had amplitudes less than 0.5 mV. In this small sample we did not  
96 observe statistical difference in the EPSP amplitudes (Fig 1E,F) between groups (KW  $p = 0.07$ )  
97 although the median Rorb EPSP ( $0.312 \pm 0.485$  mV) was more than 2 times larger than the  
98 median Tlx3 EPSP ( $0.142 \pm 0.231$  mV). This was likely driven by the heterogeneity in single  
99 pulse responses within groups; the range of amplitudes for layer 2/3 (0.032 - 0.902 mV), Rorb  
100 ( $0.105 - 1.626$  mV), Sim1 (0.068 - 1.254 mV), and Tlx3 (0.02 - 0.833 mV) spanned an order of  
101 magnitude (we could not assess the range of recurrent Rorb or Ntsr1 connections due to the  
102 low number of connections measured). The mean EPSP amplitude was consistently larger than  
103 the median (Table 2), likely due to a skewed (long-tailed) distribution of response amplitudes. A  
104 similar observation in the rat visual cortex, and mouse somatosensory cortex, has led to the  
105 suggestion that rare, large-amplitude connections are important for reliable information  
106 processing (Song et al 2005, Lefort 2009, Cossell et al. 2015). The majority of EPSP latencies  
107 were less than 2.5 ms, and similar across populations (KW  $p = 0.17$ ), consistent with a direct,  
108 monosynaptic connection between recorded neurons.

109 We could not directly quantify synaptic failures and thus calculated the coefficient of variation of  
110 synaptic amplitudes (CV; Fig 1F) to assess release probability. The CV of each connection  
111 describes the variability in a particular response in relation to the mean (ratio of standard  
112 deviation to mean) and is negatively correlated with release probability (Markram et al, 1997).  
113 The range of coefficient of variation in our data suggests differences in release probability  
114 across cells as well as between cell types (KW  $p = 0.02$ ). This is consistent with STP modeling  
115 results (see Fig 6).

116 **Table 2: Mouse single-pulse response properties (median, except where indicated)**

Connection Type/Feature	L2/3	Rorb	Sim1	Tlx3
Amplitude (mV $\pm$ SD)	$0.260 \pm 0.306$	$0.312 \pm 0.485$	$0.326 \pm 0.499$	$0.142 \pm 0.231$
Amplitude mean (mV $\pm$ SD)	$0.342 \pm 0.092$	$0.544 \pm 0.140$	$0.520 \pm 0.121$	$0.236 \pm 0.058$
Latency (ms $\pm$ SD)	$1.484 \pm 0.945$	$1.313 \pm 0.604$	$1.861 \pm 0.745$	$1.812 \pm 0.971$
Rise Time (ms $\pm$ SD)	$1.240 \pm 0.528$	$1.320 \pm 0.967$	$1.905 \pm 1.046$	$1.440 \pm 1.425$
CV ( $\pm$ SD)	$0.549 \pm 0.142$	$0.587 \pm 0.228$	$0.358 \pm 0.189$	$0.513 \pm 0.174$

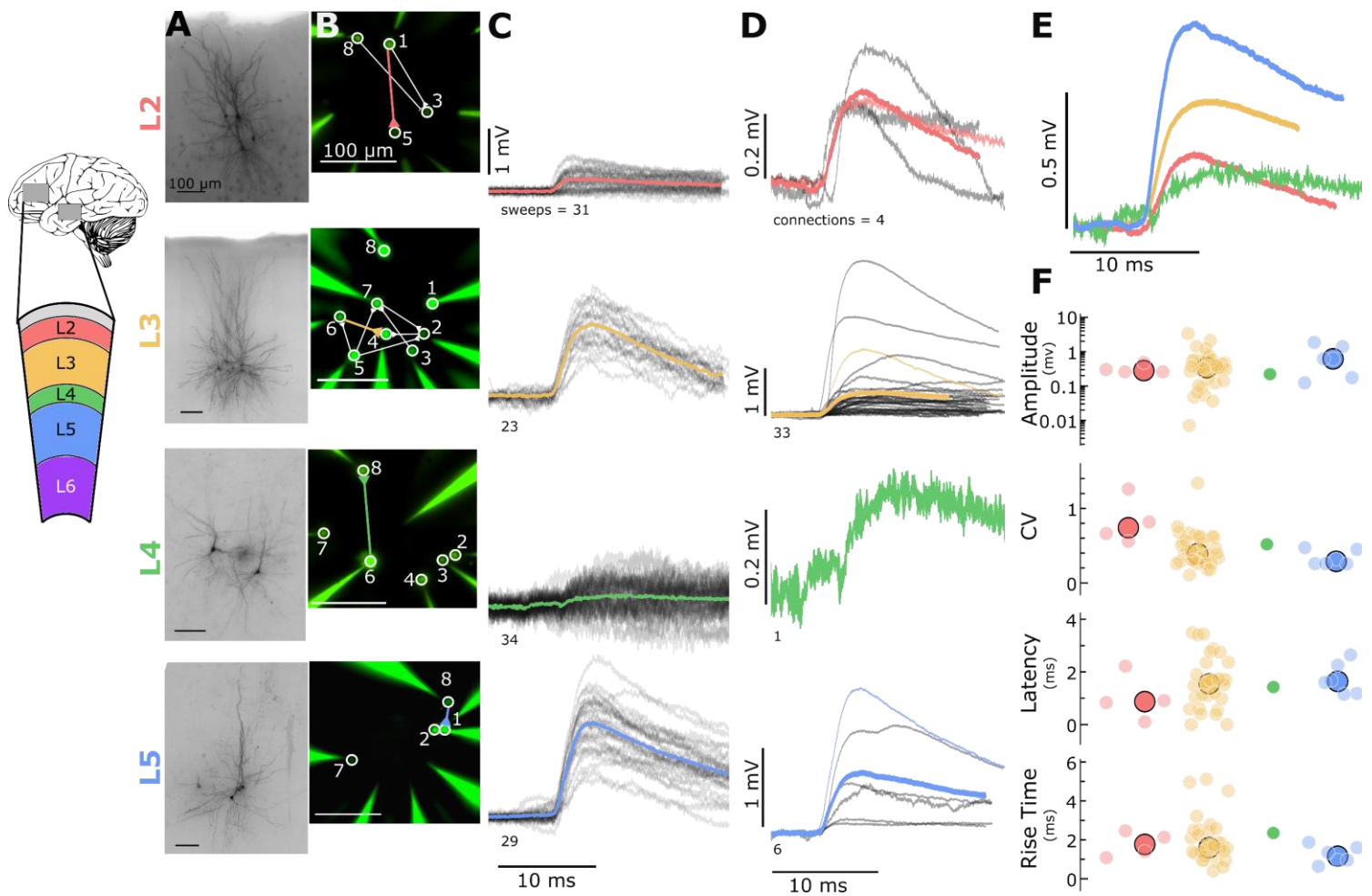
117

118

## 119 Properties of intralaminar excitatory synaptic signaling in human cortex

120 To what extent is recurrent connectivity in mouse V1 representative of connectivity in other  
121 regions and species? To make this comparison, we performed multipatch recordings in human  
122 surgical specimens from temporal and frontal cortex. We sampled recurrent intralayer  
123 connectivity in all layers containing pyramidal cells. Excitatory cells were identified either by the  
124 polarity of the synaptic currents evoked by stimulating the cell or by their morphology visualized  
125 via biocytin (Fig 2A) or fluorescent dye (Fig 2B). We found 4 connections between layer 2  
126 pyramidal cells (38 probed), 42 connections between layer 3 pyramidal cells (187 probed), 2  
127 connections between layer 4 pyramidal cells (38 probed), and 9 connections between layer 5  
128 pyramidal cells (69 probed). We did find one connection in layer 6 but have not probed this layer  
129 sufficiently to say more (2 probed connections). Human cortex had a higher connectivity rate  
130 and mean amplitude (Fig 2C, D) compared to mouse cortex (despite a higher  $[Ca]_e$  in mouse),  
131 consistent with previous reports (Molnar et. al 2008). Layers 2, 3, and 5 had a sufficient number  
132 of connections to characterize strength and kinetics however, we found no significant  
133 differences in response properties between layers (amplitude  $p=0.51$ , latency  $p=0.24$ , rise time  
134  $p=0.13$ , Table 3). We did observe differences in CV between layers 2, 3, and 5 ( $p=0.03$ , Table  
135 3) suggesting layer-specific differences in release probability of recurrent connections, similar to  
136 findings in mouse V1.

137 It is reasonable to question if the recurrent connections we see in the human are related to the  
138 disease etiology. Although we cannot rule this out, we saw no significant differences in overall  
139 connectivity between tumor and epilepsy derived specimens ( $p = 0.833$ , Fisher's Exact Test).  
140 We also found recurrent connections across multiple cortical regions and disease states in the  
141 human. Taken together, this may indicate that our results capture a common architecture of the  
142 mouse and human microcircuit.



144 **Table 3: Human single-pulse response properties (median, except where indicated)**

Connection Type/Feature	L2	L3	L5
Amplitude (mV $\pm$ SD)	0.280 $\pm$ 0.092	0.342 $\pm$ 0.660	0.615 $\pm$ 0.632
Amplitude mean (mV $\pm$ SD)	0.301 $\pm$ 0.092	0.549 $\pm$ 0.660	0.835 $\pm$ 0.632
Latency (ms $\pm$ SD)	0.871 $\pm$ 0.764	1.555 $\pm$ 0.989	1.639 $\pm$ 0.542
Rise Time (ms $\pm$ SD)	1.765 $\pm$ 0.552	1.600 $\pm$ 1.180	1.155 $\pm$ 0.419
CV ( $\pm$ SD)	0.740 $\pm$ 0.267	0.393 $\pm$ 0.228	0.290 $\pm$ 0.092

145

146 Detection limit of synaptic responses

147 When using whole cell recordings to characterize synaptic connectivity, a major limitation is that  
148 some synaptic currents may be too weak to be detected at the postsynaptic soma. Detection  
149 limits are influenced by the kinetics of PSPs, the duration of the experiment (number of  
150 averaged pulse-responses), and the amplitude and kinetics of background noise, including the  
151 properties of spontaneous PSPs. Worse, we lack even a basic estimate of the fraction of  
152 synapses that could be missed. For this reason, measurements of connectivity from multipatch  
153 experiments should be considered lower-bound estimates. Additionally, apparent connectivity  
154 may be systematically biased by cell type differences in synaptic strength, making it more  
155 difficult to interpret any measured differences in connectivity.

156

157 To address these issues, we simulated EPSPs of varying, known strength, and used a machine  
158 classifier to measure the probability that synapses could escape detection (see Methods). For  
159 each putative connection probed, we estimated the minimum PSP amplitude that could be  
160 detected. When compared to the measured amplitudes of detected PSPs, it is apparent that our  
161 data set does contain false negatives (Fig 3A, area under red dashed line). The classifier was  
162 trained to detect connections based on features previously extracted from the averaged pulse  
163 response (Fig 3B) and from the distributions of features measured on individual pulse  
164 responses (Fig 3C). Using background recording data from the postsynaptic cell, we then  
165 generated several sets of artificial pulse responses and measured the probability that the  
166 classifier would detect these, while varying the rise time and mean amplitude of the PSPs (Fig  
167 3D).



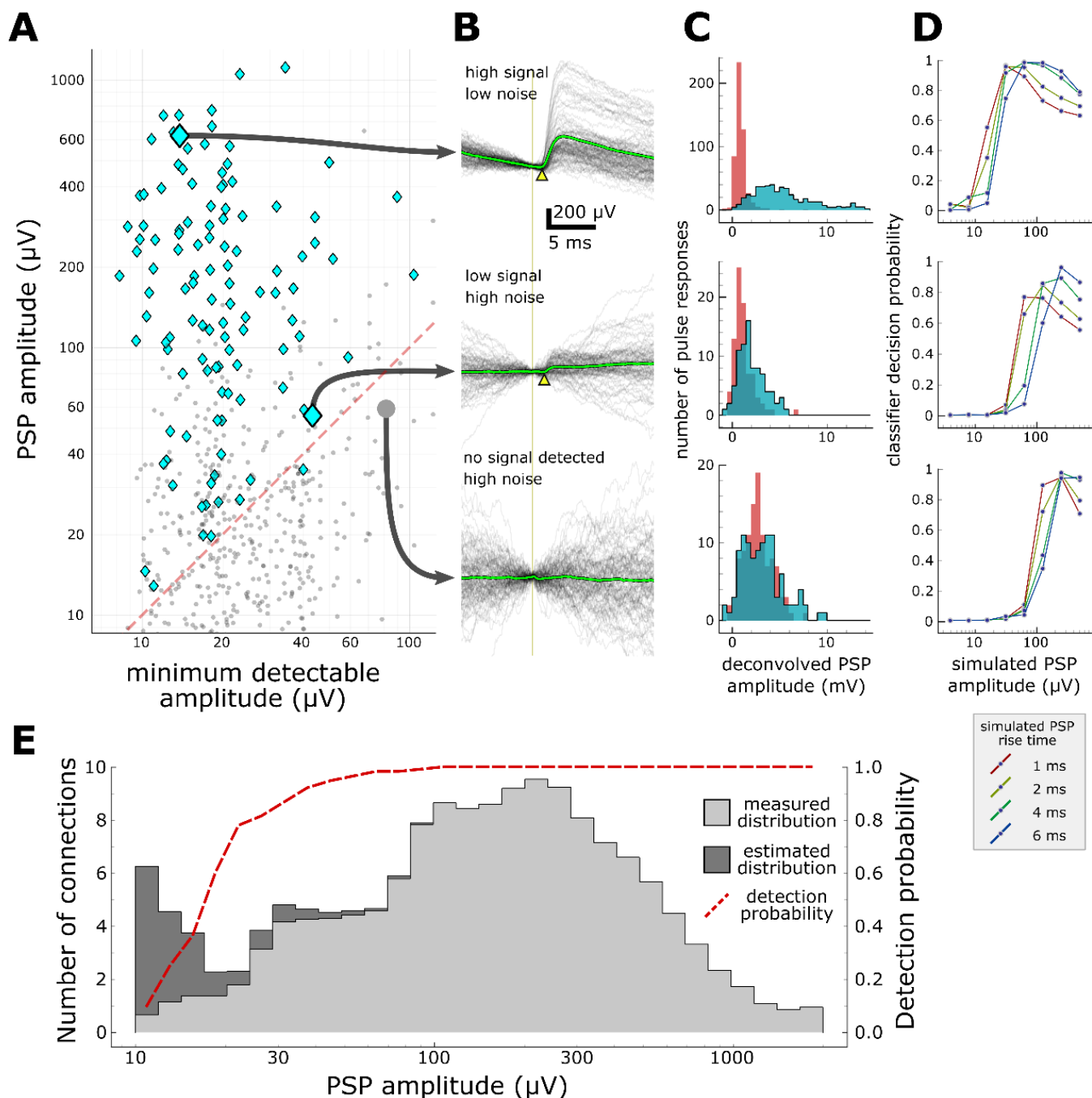


**Figure 3.** Characterization of synapse detection limits. **A.** Scatter plot showing measured PSP amplitude versus minimum detectable amplitude for each tested pair. Detected synapses (manually annotated) are shown as blue diamonds; pairs with no detected synaptic currents are grey dots. The region under the red dashed line denotes the region in which synaptic connections are likely to be misclassified as unconnected. Three example putative connections are highlighted in A and described further in panels B-D. One connection (top row) was selected for its large amplitude PSP and low background noise. Another connection (middle row) is harder to detect (PSP onset marked by yellow arrowhead) due to low amplitude and high background noise. The bottom row shows a recorded pair that was classified as unconnected. **B.** A selection of postsynaptic current clamp recordings in response to presynaptic spikes. Each row contains recordings from a single tested pair. The vertical line indicates the time of presynaptic spikes, measured as the point of maximum  $dV/dt$  in the presynaptic recording. Yellow triangles indicate the onset of the PSP. **C.** Histograms showing distributions of peak response values measured from deconvolved traces (see Methods). Red area indicates measurements made on background noise; blue area indicates measurements made immediately following a presynaptic spike. **D.** Characterization of detection limits for each example. Plots show the probability that simulated PSPs would be detected by a classifier, as a function of the rise time and mean amplitude of the PSPs. Each example has a different characteristic detection limit that depends on the recording background noise and the length of the experiment. **E.** An estimate of the total number of false negatives across the entire dataset. The measured distribution of PSP amplitudes is shown in light grey (smoothed with a gaussian filter with  $\sigma=1$  bin). The estimated correction show in dark grey is derived by dividing the measured distribution by the overall probability of detecting a synapse (red dashed line) at each amplitude.

169 With this approach, we can place constraints for any given experiment on the properties of  
170 putative missed synaptic connections. Recordings with low background noise and adequate  
171 averaging will generally allow the detection of very small synaptic currents (Fig 3D, top panel  
172 has a detection limit 10-20  $\mu\text{V}$ ), whereas lower quality recordings will have higher detection  
173 thresholds and will report lower connectivity rates (Fig 3D, bottom panel has a poor detection  
174 limit near 100  $\mu\text{V}$ ). Likewise, PSPs with shorter rise time (or other properties that distinguish the  
175 PSP from background) are more likely to be detected (Fig 3D). These results suggest that the  
176 differences in experimental protocol between studies (for example, the amount of averaging  
177 done for each connection) can have a substantial impact on the apparent connectivity reported,  
178 but also that future studies could reconcile these differences by carefully characterizing their  
179 detection limits.

180 The results in Figure 3A suggest another tantalizing opportunity: if we know the area that  
181 contains false negatives (under the red dashed line) and the density of true positives above the  
182 line, then we can make a first-order estimate of the number of connections that were missed  
183 across a series of experiments. Figure 3E shows the distribution of PSP amplitudes across all  
184 detected synapses (light grey area) as well as the curve representing the probability that  
185 synapses would be detected at any amplitude. Dividing the measured distribution by the  
186 probability of detection yields a corrected distribution (dark grey) with an overall 10% increase in  
187 connectivity. Although it is clear that this estimate becomes unstable as the detection probability  
188 approaches zero, a surprising result of this analysis is that, for moderate amplitudes of 20-100  
189  $\mu\text{V}$ , we expect to see very few false negatives. Depending on the expected prevalence of  
190 weaker connections < 20  $\mu\text{V}$ , this hints that our current sampling methods may be adequate to  
191 detect the vast majority of synaptic connections. We should be cautious, however, in our  
192 interpretation of this result--the analysis relies on several assumptions about the behavior of the  
193 classifier and the realism of the simulated PSPs. Ultimately, the approach must be validated  
194 against a larger dataset.

## 195 Connection probability of excitatory synapses

196 Estimates of connectivity vary widely across studies, in part due to methodological differences.  
197 In addition to the effects of detection sensitivity described above, estimated connection  
198 probability is affected by the intersomatic distances over which connections are sampled. This  
199 spatial distribution of connections may also offer insight into the organization of functional  
200 microcircuits. In mouse, connectivity in layer 2/3, Rorb, and Sim1 neurons within 100  $\mu\text{m}$  was  
201 similar (~10%; Fig 4, left; connected/probed, L2/3: 17/178, Rorb: 19/205, Sim1: 49/507).  
202 However, within this range, Tlx3 connectivity was markedly lower (~4%; Tlx3: 32/818.). Ntsr1  
203 connectivity was significantly more sparse as only one connection was detected (out of 312  
204 probed) at a distance of 163  $\mu\text{m}$  ( $p < 0.05$  relative to all other groups). Most connectivity versus  
205 distance profiles (Fig 4B) showed a progressive reduction in the connection probability with  
206 increasing distance.

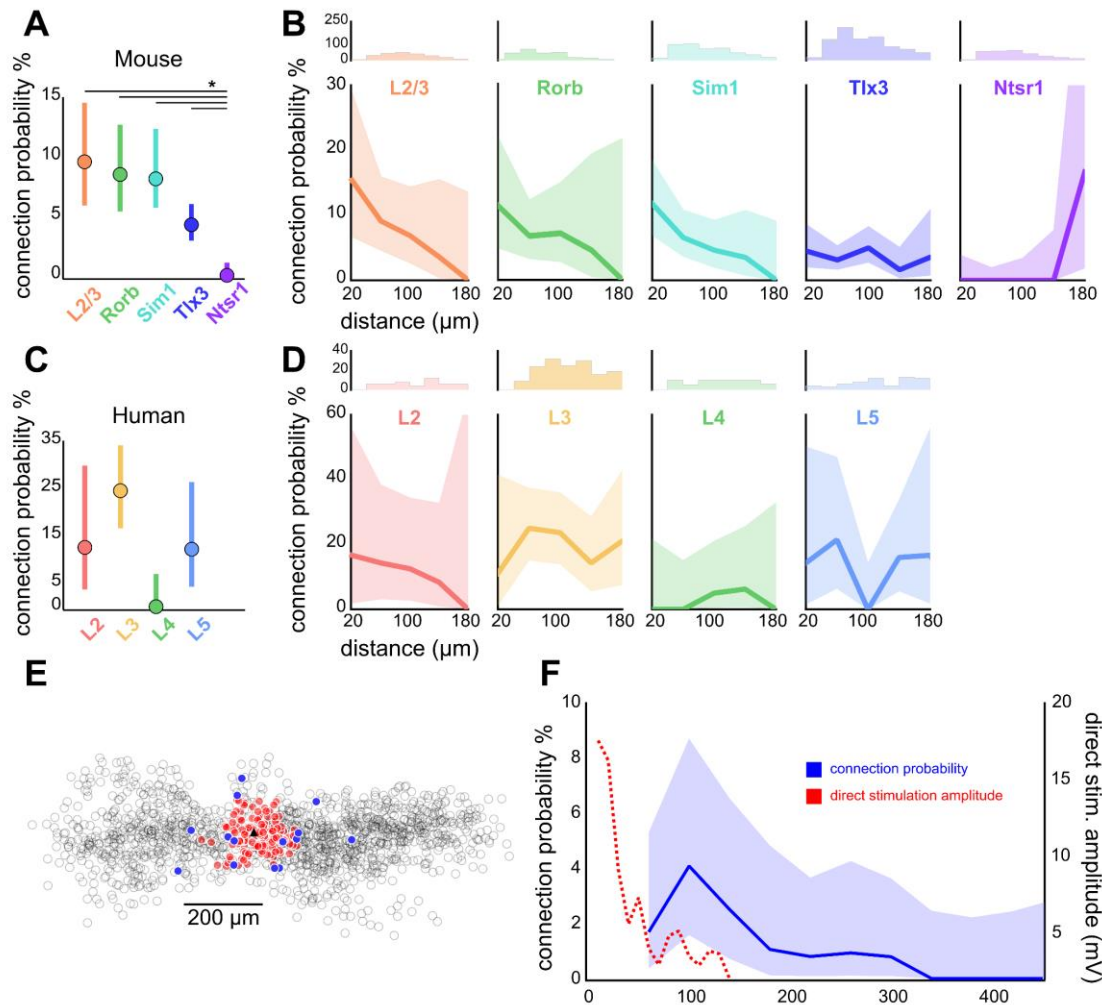


**Figure 4.** Distance dependent connectivity profiles of mouse and human E-E connections. **A.** Recurrent connection probability and distribution of connections for mouse Cre lines and layer 2/3. Mean connection probability (filled circles) and 95% confidence intervals (bars) for connections probed within 100  $\mu\text{m}$ . Asterisk (\*) indicates p-value <0.05 (Bonferroni corrected). **B.** Connection probability over distance for mouse Cre lines and layer 2/3. *Top:* Histogram of putative connections probed. *Bottom:* Mean connection probability (thick line) with 95% confidence intervals (shading). **C.** Like-to-like connection probability and distribution of connections between human pyramidal neurons. Mean connection probability (filled circles) and 95% confidence intervals (bars) for connections probed within 100  $\mu\text{m}$ . **D.** Connection probability over distance for human pyramidal neurons, formatted as in panel B. **E.** Tlx3-Tlx3 connection probability measured by two-photon mapping. X-Y distance distribution of connections probed onto a postsynaptic cell (black triangle), detected presynaptic neurons (filled circles), no connection detected (empty circles), and direct event artifact due to undesired activation of opsin in the dendritic arbor of the recorded cell (red circles). **F.** Connection probability and stimulation artifact over distance measured by two-photon mapping. Mean connection probability vs. distance (blue line; starting at 50  $\mu\text{m}$ ) with 95% confidence intervals (shading) and direct event artifact amplitude vs. distance (dotted red line) for Tlx3-Tlx3 connections probed with two-photon stimulation.

208 Utilizing a multipatch technique limits our ability to probe connectivity at high density and far  
209 distances. Two-photon optogenetic stimulation, which allows for focal stimulation of many  
210 (mean=57 cells, range=8-117) presynaptic cells in a single experiment, and critically, enables  
211 the intersomatic distance between those cells to be greater than is generally feasible with  
212 multipatch experiments, was used to overcome these limitations. ReaChR expressing Tlx3-Cre  
213 neurons in layer 5 were photo-stimulated while one or two putative postsynaptic cells were  
214 monitored in whole-cell current clamp configuration (Fig 4E). With this technique, using 9 mice,  
215 we found a similar connection probability over the distance range of multipatch experiments  
216 (4/167, 2.40%) and reduced connectivity at extended distances up to 785  $\mu\text{m}$  (Fig 4E; 10/1290,  
217 0.78%) with the furthest connection found at 300  $\mu\text{m}$ .

218 Overall, connectivity in human cortex was significantly higher than that in mouse (human 19%,  
219 mouse 6.8%, Fisher's  $p < 0.001$ ). In human cortex, layer 2 and layer 5 connectivity showed  
220 similar connection probability (~12%; layer 2: 3/24; layer 5: 4/33; Fig 4C), while layer 3 recurrent  
221 connectivity was approximately double (24%, 22/90). More data is needed to accurately resolve  
222 the distance dependence of recurrent connectivity in the human (Fig 4D).

### 223 Short-term plasticity of excitatory synapses

224 For a subset of synaptic connections in mouse cortex (Fig S1G), we characterized the short-  
225 term synaptic dynamics. We probed short-term dynamics with stimulus trains consisting of eight  
226 pulses to induce STP, followed by a delay and four more pulses to measure recovery (Fig 5A,  
227 left). The eight initial pulses allowed responses to reach a steady state, from which we could  
228 characterize the extent of depression (or facilitation) at frequencies from 10 - 100 Hz. The 50 Hz  
229 stimulation protocol had additional recovery intervals ranging from 250 - 4000 ms (Fig 5A, right).  
230 Figure 5B shows average synaptic responses to a 50 Hz stimulus with 8 initial pulses followed  
231 by 4 pulses at a 250 ms delay from individual Sim1-Sim1 connections shown in grey, and the  
232 grand average overlaid (cyan). We used exponential deconvolution (Fig 5B, middle; Eq. 2) to  
233 estimate the amplitudes of individual PSPs in the absence of temporal summation (arising from  
234 the relatively long cell membrane time constant).

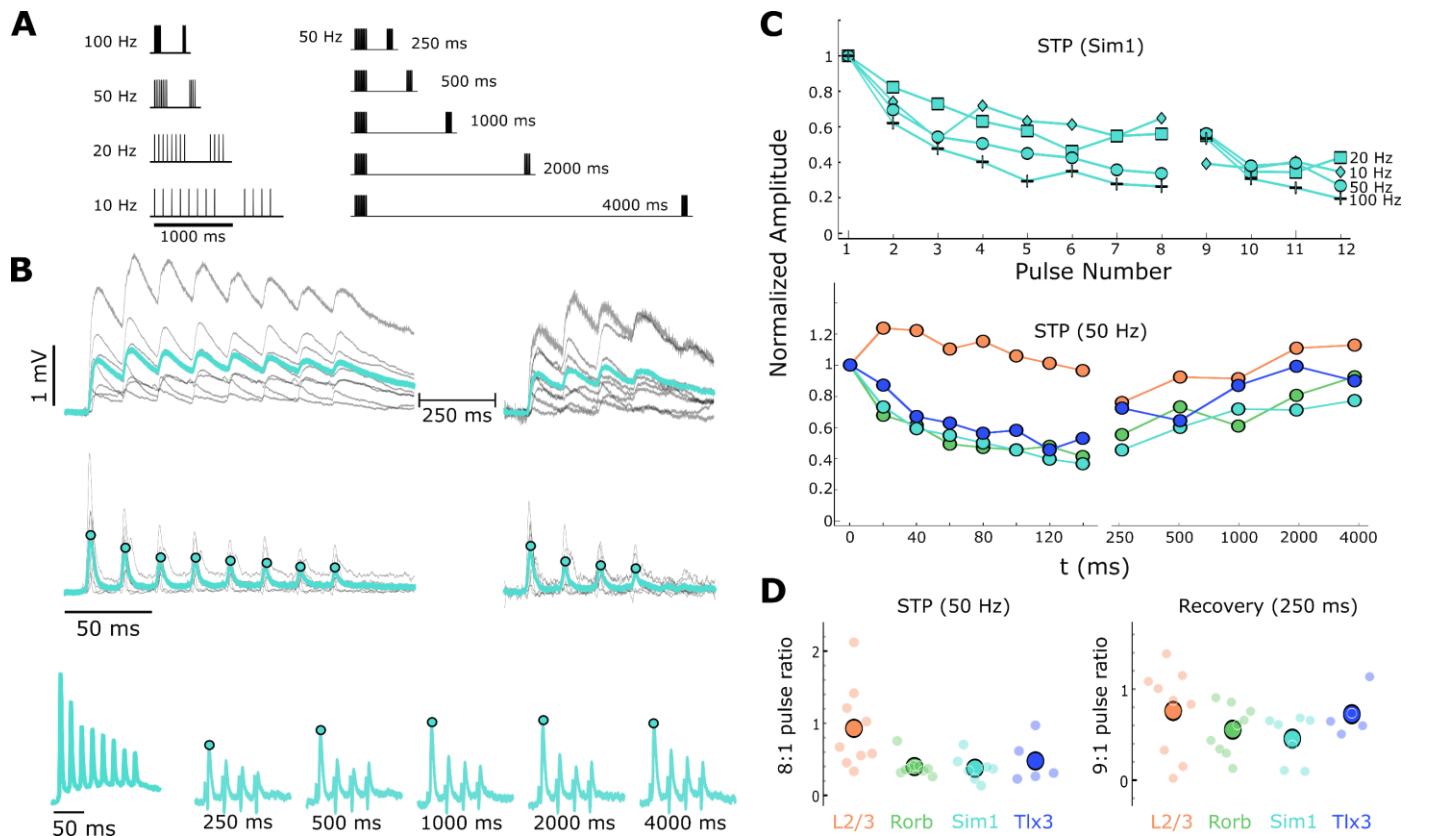


**Figure 5.** Short-term dynamics of mouse recurrent connections by Cre-type and layer. **A.** Schematic of STP and STP recovery stimuli. **B.** Sim1-Cre EPSPs in response to a 50 Hz stimulus train (top; 8 induction pulses and 4 recovery pulses delayed 250 ms; individual connection: gray traces; blue: Sim1-Cre average EPSP at 50Hz). Exponential deconvolution followed by lowpass filter of EPSPs above (middle, filled circles: pulse amplitudes in C.). Exponential deconvolution of 50 Hz stimulus with all 5 recovery time points in A (bottom, filled circles: pulse amplitudes in C.). **C.** The mean normalized amplitude of deconvolved response versus pulse number at multiple stimulation frequencies for Sim1-Cre (top). Normalized amplitude of the deconvolved response at 50 Hz with first recovery pulse at each interval for each Cre-type and L2/3 connections (bottom). **D.** The depth of depression during 50Hz induction (left) as measured by the amplitude ratio of the 8th to 1st pulse for each Cre-type and layer (small circles) and grand mean (large circles). Amount of recovery at 250 ms latency (right) for each Cre-type and layer (small circles) and grand mean (large circles).

235 We measured the peak amplitude of the deconvolved response for every pulse (cyan dots) and  
 236 normalized to the first pulse in the train in order to characterize short-term dynamics across four  
 237 frequencies. Fig 5C (top) highlights frequency dependent depression in recurrent Sim1  
 238 connections. We similarly measured recovery from short-term effects at various time delays (Fig  
 239 5B, bottom, cyan dots) for layer 2/3, Rorb, Sim1, and Tlx3 connections (Fig 5C, bottom). A  
 240 simple analysis of the magnitude of, and recovery from, short-term plasticity is shown in Fig 5D.  
 241 The amplitude ratio of the last pre-recovery interval pulse (8) to the first shows that layer 2/3  
 242 exhibits less depression than Rorb, Sim1, and Tlx3 (Fig 5D, left). All types showed a similar  
 243 time-course of recovery as measured by the ratio of the first recovery pulse (9) to the first  
 244 induction pulse (Fig 5D, right). Recovery also tended to be rapid in the first 250 ms followed by  
 245 a slower, incomplete recovery measured at 4 seconds (Fig 5C, middle).

246 To better capture the dynamic processes contributing to short-term plasticity and how they may  
 247 differ among connection types we turned to a model of short-term dynamics which has been  
 248 well described (Hennig, 2013; Mongillo et al., 2008; Richardson et al., 2005). Rorb, Sim1, and  
 249 Tlx3 synapses were modelled with depression (Eq. 4, methods) and use-dependent  
 250 replenishment (Eq. 5, methods). This model performed well (Fig 6A, Sim1 connections  $r^2 =$   
 251 0.845, Table 4) in capturing depression during the 8 initial pulses at various frequencies (Fig 6A)  
 252 as well as modeling recovery at various delays (Fig 6A, circles). From this model we can extract  
 253 free parameters such as  $P_0$  which describes release probability and  $\tau_{r0}$  which describes the time  
 254 course of recovery from depression. Rorb connections had the largest release probability ( $P_0 =$   
 255 0.30, Fig 6B, left) which is consistent with faster entry into depression (Fig 5C, bottom pulse 2).  
 256 Conversely, Tlx3 connections had a lower initial release probability ( $P_0 = 0.16$ ) and recovered  
 257 more quickly ( $\tau_{r0} = 0.736$  s). Table 4 shows full results of the model across these 3 types as well  
 258 as calculated paired Z-scores (Eq. 6) for  $P_0$  and  $\tau_{r0}$ . The heterogeneity in layer 2/3 response  
 259 dynamics made it difficult to constrain the model and thus were not included in this analysis.  
 260

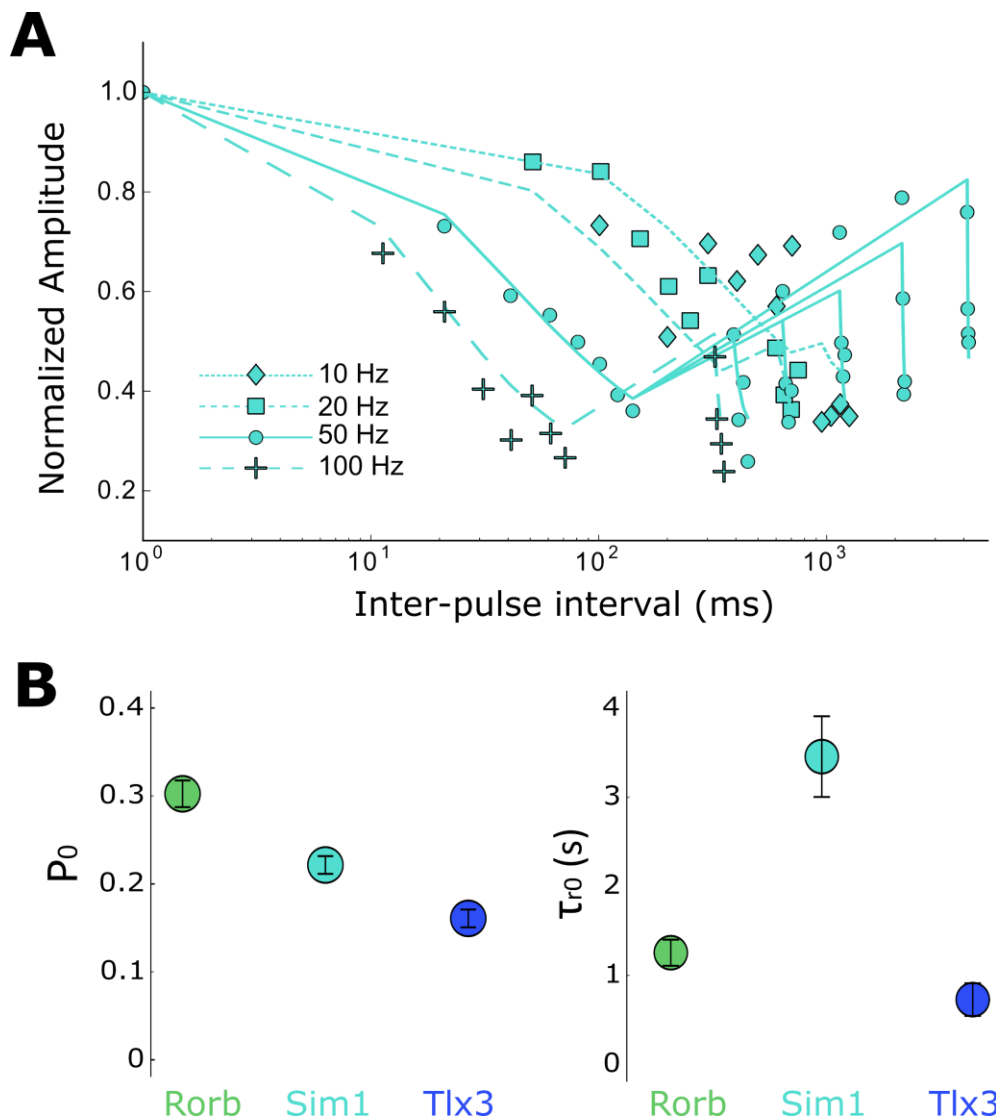


**Figure 6.** Modeling of short-term depression in recurrent Rorb, Sim1, and Tlx3 connections. **A.** Sim1 Cre average dynamic response; Same data as in Fig 5C, top plotted on a log-X time scale with modeling fits overlaid. **B.** Results of model for parameters  $P_0$  and  $\tau_{r0}$ . Values are means with standard error of the covariance matrix. Paired Z-scores (Eq. 6) in Table 4.

261 **Table 4: Model of short-term dynamics**

Connection Type/Model Parameter	Rorb	Sim1	Tlx3
$\tau_{r0}$ (sec $\pm$ SE)	1.26 $\pm$ 0.292	3.45 $\pm$ 0.901	0.736 $\pm$ 0.365
$P_0$ ( $\pm$ SE)	0.30 $\pm$ 0.03	0.22 $\pm$ 0.02	0.16 $\pm$ 0.02
$\tau_{FDR}$ (ms $\pm$ SE)	130.6 $\pm$ 56.8	281.0 $\pm$ 128.1	179.3 $\pm$ 173.1
$\alpha_{FDR}$ ( $\pm$ SE)	0.85 $\pm$ 0.09	0.75 $\pm$ 0.11	0.40 $\pm$ 0.13
$r^2$	0.836	0.845	0.687
Rorb Z-score	$P_0$ / $\tau_{r0}$	2.31	1.12
Sim1 Z-score	2.02	$P_0$ / $\tau_{r0}$	2.79
Tlx3 Z-score	3.55	2.12	$P_0$ / $\tau_{r0}$

262

## 263 Discussion

264 We leveraged the sub-millisecond sampling, high gain, and low noise of multipatch recordings  
 265 to investigate the functional connectivity and short-term dynamics of recurrent synapses in the  
 266 adult mouse and human cortex. We observed sparse recurrent connections between excitatory  
 267 neurons in layers 2/3 through 6 in adult mouse visual cortex and layers 2 through 6 of adult  
 268 human cortex. We supplemented mouse multipatch experiments with high throughput 2P  
 269 optogenetic stimulation to sample connectivity at greater distances than is generally feasible  
 270 using the multipatch approach. The large majority of excitatory recurrent connections in mouse  
 271 cortex exhibited short-term synaptic depression.

272 Recordings made from *in vitro* slice preparations offer a unique combination of temporal  
 273 resolution, low resistance intracellular access, and long term stability. Although these features  
 274 provide an excellent environment for multipatch recordings, there are also associated limitations  
 275 that must be considered carefully. Estimates of connectivity derived from multipatch  
 276 experiments in brain slices should be considered as a lower bound on the underlying population  
 277 connectivity due to sensitivity to false negatives from several sources. These effects may  
 278 contribute to differences in reported connectivity across studies. A fraction of synaptic  
 279 connections are expected to be severed during slicing; one estimate of connectivity perturbed  
 280 by slicing approaches 50% (Levy and Reyes 2012). The effect on measured connection

281 probability depends on the thickness of the slice, the depth of recorded cells from the cut  
282 surface, the morphology of recorded cells, and the distance between them. Although we  
283 minimize lost connections by patching deep in the slice (>40  $\mu\text{m}$ ) and by selecting cells in close  
284 proximity, this is still a likely source of false negatives in our data. Another fraction of synapses  
285 are expected to be either too weak (Isaac et al 1995) or too distal from the recording pipette to  
286 be detected. The magnitude of this effect is difficult to estimate, but our initial analysis hints that  
287 our methods are sensitive enough to capture the majority of synapses. To obtain more accurate  
288 estimates of connectivity, it will be necessary to combine these results with other methods such  
289 as *in vivo* multipatch recordings, transsynaptic tracing, and serial section electron microscopy.  
290 These methods are also limited, but in each case the constraints are different and potentially  
291 complementary.

292 There is a wide range of reported rates of recurrent connectivity among excitatory neurons in  
293 rodent studies. One suggestion is that differences between the juvenile and adult rodent can  
294 explain the variance (Jiang et al. 2016). To avoid changes associated with development, we  
295 carried out our experiments in the adult (about two months old) cortex. Nevertheless, our  
296 conclusion that recurrent connectivity is sparse but not absent is similar to results from  
297 experiments in other adult (Cossell et al. 2015, Lee et al. 2016) and juvenile animals (Mason et  
298 al. 1991, Holmgren et al. 2003, Song et al. 2005, Sjostrom et al. 2001, Morishima et al. 2011,  
299 Perin et al. 2011, Lefort et al. 2009, Levy and Reyes 2012). A notable difference, however, is  
300 that we never observed rates of recurrent connectivity as high or synaptic amplitudes as large  
301 as those reported in juvenile rodents, consistent with the observation that the rate of recurrent  
302 connectivity and synaptic strength declines with age (Burgeois and Rakic 1993, Reyes and  
303 Sackman 1999).

304 Different rates of recurrent connectivity across neuronal classes may suggest a mechanism for  
305 observed differences in their functional influence on downstream targets. In this context, it is  
306 interesting that in the mouse, all three classes of deep projection neuron had different rates of  
307 recurrent connectivity. This was approximately 10% in Sim1 (layer 5; subcortically projecting)  
308 expressing cells, whereas Tlx3 expressing neurons (layer 5; intracortically projecting)  
309 interconnect approximately half as frequently (~4%). Relatively high rates of recurrent  
310 connectivity are not a generalizable property of subcortically projecting cells, as Ntsr1  
311 expressing cells (layer 6) had the lowest rate of intralaminar connectivity among all excitatory  
312 cell types tested here.

313 How do the rates of recurrent connectivity in mouse compare to other species? In human  
314 cortex, we and others (Molnar et al. 2008) find that the frequency of connectivity among layer 3  
315 excitatory neurons is at least two and half times greater than the highest connectivity rate  
316 observed in the adult mouse. It may be that high rates of recurrent connectivity in layer 3 are a  
317 circuit feature of higher mammals as this is also reported to be the case in cat and monkey  
318 (Kisvarday et al 1986, McGuire et al 1991, Bopp et al 2014). Future work will examine how  
319 short-term dynamics and/or inhibitory feedback may counterbalance recurrent excitatory  
320 connectivity to prevent runaway excitation.



321 In our study, the distance dependent connection probability profiles observed in all excitatory  
322 types appear to fall off with distance and are consistent with connectivity depending on the  
323 extent of overlap between neighboring axons and dendrites (Peters 1979, Binzegger et al. 2004,  
324 Braitenberg and Schüz 1998, van Pelt and van Ooyen 2013). It is unlikely that the distance  
325 dependent connectivity profiles we observed are an artifact of tissue preparation as it has  
326 previously been demonstrated that the truncation of neuronal processes reduces overall  
327 connectivity but maintains the spatial pattern of connections (Stepanyants et al. 2009, Levy and  
328 Reyes 2012). Additionally, 2P optogenetic experiments allowed for interrogating potential  
329 connections at much larger distances. Further effort is needed to determine whether our  
330 connectivity profiles can be predicted from neuronal morphology.

331 Recurrent excitatory synapses most commonly exhibit short-term depression (Markram 1997,  
332 Reyes and Sackmann 1999, Lefort and Petersen 2017), which is thought to normalize the  
333 synaptic gain across different firing frequencies (Abbott et al. 1997) as well as minimize  
334 runaway excitation within recurrent circuit elements. In our sample, the rate of entry into  
335 depression varied among Cre types, which suggests differences in initial release probability. In  
336 support of this hypothesis, we also observed that Tlx3 expressing neurons exhibited the slowest  
337 entry into depression had the smallest initial EPSP amplitudes and a relatively high CV.  
338 Nevertheless, the short-term dynamics of the Cre expressing neurons were uniformly  
339 depressing, and their maximal depression was also similar. In contrast, layer 2/3 pyramidal cell  
340 STP was more evenly distributed between facilitating and depressing. This is in agreement with  
341 a previous study by Lefort and Petersen (2017). Although less common, facilitation in recurrent  
342 excitatory synapses has also been observed in the medial prefrontal cortex and is hypothesized  
343 to play a role in reverberant activity (Wang et al. 2006).

344 Ultimately, we seek a description of the cortical circuit from which mechanistic computational  
345 models can be built and hypotheses about cortical function can be tested. Although many parts  
346 of the circuit have been described in the past, incompatibilities between experiments have made  
347 it difficult to assemble a complete, coherent picture of the whole. We have taken steps toward  
348 ensuring that our results can be interpreted in the context of future experiments, but more work  
349 is needed to generate a consistent description of the cortical circuit. To that end, we have begun  
350 a large-scale project to replicate these measurements across a wider variety of cell types in the  
351 mouse and human cortex; the results of our early-stage data collection presented here suggest  
352 that systematic and standardized characterization will provide a detailed, quantitative, and  
353 comprehensive description of the circuit wiring diagrams and will facilitate the investigation of  
354 circuit computation.

## 355 **Methods**

### 356 Animals and Tissue Preparation

357 Adult mice of either sex (mean age P45 ± 4; SD) were housed and sacrificed according to  
358 protocols approved by the Institutional Care and Use Committee at the Allen Institute (Seattle,  
359 WA), in accordance with the National Institutes of Health guidelines. Transgenic mouse lines

360 were used for experimentation and chosen based on cortical layer specific expression and/or  
361 known projection patterns. In the following mouse lines, subpopulations of excitatory neurons  
362 are selectively labelled with fluorescent reporters (tdTomato or GFP): Tlx3-Cre\_PL56;Ai14  
363 (n=57), Sim1-Cre\_KJ18;Ai14 (n=20), Rorb-T2A-tTA2;Ai63 (n=28), Ntsr1-Cre\_GN220;Ai140  
364 (n=10) (Allen Institute; see also <http://connectivity.brain-map.org/transgenic>). Two drivers, Sim1-  
365 Cre (subcortical projecting; CS or PT type; Allen Brain Atlas, <http://connectivity.brain-map.org/>)  
366 and Tlx3-Cre, (corticocortical projecting; CC or IT type; Kim et al 2015), were used to label layer  
367 5 pyramidal cells, in order to sample projection-specific subpopulations. For optogenetic  
368 experiments, Tlx3-Cre driver mice were bred with ROSA26-ZtTA/J mice (Jackson Laboratory)  
369 and Ai136 mice (Daigle et. al 2017), in which a fusion of the ReaChR opsin (Lin 2013) with  
370 EYFP is expressed from the TIGRE locus (Zeng et al. 2008) in a Cre- and tTA-dependent  
371 manner. Previous studies have emphasized the differences in cortical connectivity particularly at  
372 older ages. To assess whether age impacted the results reported here, a subset of experiments  
373 were repeated for Sim1 connections in older mice (mean age  $61 \pm 1$ ; SD, n=10). We saw no  
374 difference in recurrent connectivity rate (<100  $\mu\text{m}$ ; P40-60: 36/423, >P60: 15/269, Fisher's  $p =$   
375 0.23) or response amplitude (P40-60:  $0.53 \pm 0.12$  mV, >P60:  $0.59 \pm 0.2$  mV,  $p = 0.98$  KS test)  
376 among across the two time points.

377 Animals were deeply anesthetized with isoflurane and then transcardially perfused with ice-cold  
378 oxygenated artificial cerebrospinal fluid (aCSF) containing (in mM): 98 HCl, 96 N-methyl-d-  
379 glucamine (NMDG), 2.5 KCl, 25 D-Glucose, 25 NaHCO<sub>3</sub>, 17.5 4-(2-hydroxyethyl)-1-  
380 piperazineethanesulfonic acid (HEPES), 12 N-acetylcysteine, 10 MgSO<sub>4</sub>, 5 Na-L-Ascorbate, 3  
381 Myo-inositol, 3 Na Pyruvate, 2 Thiourea, 1.25 NaH<sub>2</sub>PO<sub>4</sub>·H<sub>2</sub>O, 0.5 CaCl<sub>2</sub>, and 0.01 taurine  
382 (aCSF 1). All aCSF solutions were bubbled with carbogen (95% O<sub>2</sub>; 5% CO<sub>2</sub>).

383 Acute parasagittal slices (350  $\mu\text{m}$ ) containing primary visual cortex from the right hemisphere  
384 were prepared with a Compresstome (Precisionary Instruments) in ice-cold aCSF 1 solution at a  
385 slice angle of 17° relative to the sagittal plane in order to preserve pyramidal cell apical  
386 dendrites. Slices were then allowed to recover for 10 minutes in a holding chamber (BSK 12,  
387 Scientific Systems Design) containing oxygenated aCSF 1 maintained at 34°C (Ting et al.  
388 2014). After recovery, slices were kept in room temperature oxygenated aCSF holding solution  
389 (aCSF 2) containing (in mM): 94 NaCl, 25 D-Glucose, 25 NaHCO<sub>3</sub>, 14 HEPES, 12.3 N-  
390 acetylcysteine, 5 Na-L-Ascorbate, 3 Myo-inositol, 3 Na Pyruvate, 2.5 KCl, 2 CaCl<sub>2</sub>, 2 MgSO<sub>4</sub>, 2  
391 Thiourea, 1.25 NaH<sub>2</sub>PO<sub>4</sub> · H<sub>2</sub>O, 0.01 Taurine for a minimum of one hour prior to recording.

392 Human tissue surgically resected from adult cortex was obtained from patients undergoing  
393 neurosurgical procedures for the treatment of symptoms associated with epilepsy or tumor.  
394 Data were collected from 67 total slices from 22 surgical cases (17 epilepsy, 5 tumor, mean age  
395  $40 \pm 17$  years; SD). Tissue obtained from surgery was distal to the core pathological tissue and  
396 was deemed by the physician not to be of diagnostic value. Specimens were derived from the  
397 temporal lobe (13 epilepsy, 4 tumor) and the frontal lobe (4 epilepsy, 1 tumor). Specimens were  
398 placed in a sterile container filled with prechilled (2-4°C) aCSF 3 containing decreased sodium  
399 replaced with NMDG to reduce oxidative damage (Zhao et al., 2011) composed of (in mM): 92  
400 NMDG, 2.5 KCl, 1.25 NaH<sub>2</sub>PO<sub>4</sub>, 30 NaHCO<sub>3</sub>, 20 HEPES, 25 glucose, 2 thiourea, 5 Na-  
401 ascorbate, 3 Na-pyruvate, 0.5 CaCl<sub>2</sub>·4H<sub>2</sub>O and 10 MgSO<sub>4</sub>·7H<sub>2</sub>O. pH was titrated to 7.3–7.4 with

402 HCl and the osmolality was 300-305 mOsmoles/Kg. Surgical specimens were transported (10-  
403 40 minutes) from the surgical site to the laboratory while continuously bubbled with carbogen.

404 Resected human tissue specimens were trimmed to isolate specific regions of interest, and  
405 larger specimens were cut into multiple pieces before trimming. Specimens were mounted in  
406 order to best preserve intact cortical columns (spanning pial surface to white matter) before  
407 being sliced in aCSF 3 using a Compresstome. Slices were then transferred to oxygenated  
408 aCSF 3 maintained at 34°C for 10 minutes. Slices were kept in room temperature oxygenated  
409 aCSF holding solution (aCSF 4) containing, in mM: 92 NaCl, 30 NaHCO<sub>3</sub>, 25 D-Glucose, 20  
410 HEPES, 5 Na-L-Ascorbate, 3 Na Pyruvate, 2.5 KCl, 2 CaCl<sub>2</sub>, 2 MgSO<sub>4</sub>, 2 Thiourea, 1.2  
411 NaH<sub>2</sub>PO<sub>4</sub>·H<sub>2</sub>O for a minimum of one hour prior to recording.

## 412 Electrophysiological Recordings

413 Recording slices from mouse and human tissue were processed in largely the same manner,  
414 with a key difference being the external calcium concentration used for recording. Human slices  
415 were held in aCSF containing 1.3 mM calcium while mouse slices utilized 2.0 mM calcium.  
416 Below we discuss the full preparation for slice processing as well as the rationale for this  
417 calcium difference.

418 Slices were transferred to custom recording chambers perfused (2 mL/min) with aCSF  
419 maintained at 31-33°C, pH 7.2-7.3, and 30-50% oxygen saturation (as measured in the  
420 recording chamber). aCSF (aCSF 5) contained (in mM), 1.3 or 2 CaCl<sub>2</sub> (2.0 in mouse  
421 experiments and either 1.3 or 2.0 in human experiments), 12.5 D-Glucose, 1 or 2 MgSO<sub>4</sub>, 1.25  
422 NaH<sub>2</sub>PO<sub>4</sub>·H<sub>2</sub>O, 3 KCl, 18 NaHCO<sub>3</sub>, 126 NaCl, 0.16 Na L-Ascorbate.

423 The concentration of calcium in the external recording solution affects release probability and  
424 other aspects of synaptic dynamics (Borst 2010, Pala & Petersen 2015, Jouhanneau 2015,  
425 Urban-Ciecko et al 2015). Although concentrations close to 1 mM are expected to most closely  
426 approximate *in vivo*-like synaptic dynamics, most prior multipatch studies used elevated calcium  
427 concentrations to increase the strength of synaptic currents and improve throughput. In our  
428 mouse recordings, we used 2.0 mM CaCl<sub>2</sub> to be consistent with previous connectivity studies  
429 (Markram et. al 1997, Reyes and Sakmann 1999, Perin et. al 2011, Jiang et. al 2015) and to  
430 help ensure the success of our system integration test. In a limited test among recurrent Sim1  
431 connections, the difference in synapse strength was statistically insignificant between 2.0 mM  
432 and 1.3 mM CaCl<sub>2</sub> (2.0mM CaCl<sub>2</sub> single-pulse amplitude = 501 ± 108 μV, n=9; 1.3mM CaCl<sub>2</sub> =  
433 383 ± 90 μV, n=15; KS test p = 0.47). We selected 1.3 mM [Ca<sup>++</sup>]<sub>e</sub> for our human experiments  
434 because of reports that the synaptic strength is higher than in mouse and to minimize the  
435 complex events that can be initiated by individual spikes in human tissue (Molnar et al. 2008)  
436 that make identifying monosynaptic connectivity challenging. Future mouse recordings will also  
437 be carried out at 1.3 mM [Ca<sup>++</sup>]<sub>e</sub> in order to capture the physiological synaptic dynamics.

438 Slices were visualized using oblique infrared illumination using 40x or 4x objectives (Olympus)  
439 on a custom motorized stage (Scientifica), and images were captured using a digital sCMOS  
440 camera (Hamamatsu). Pipette positioning, imaging, and subsequent image analysis were

441 performed using the python platform acq4 ([acq4.org](http://acq4.org), Campagnola et al. 2014). Eight electrode  
442 headstages (Axon Instruments) were arranged around the recording chamber, fitted with  
443 custom headstage shields to reduce crosstalk artifacts, and independently controlled using triple  
444 axis motors (Scientifica). Signals were amplified using Multiclamp 700B amplifiers (Molecular  
445 Devices) and digitized at 50-200kHz using ITC-1600 digitizers (Heka). Pipette pressure was  
446 controlled using electro pneumatic pressure control valves (Proportion-Air) and manually  
447 applied mouth pressure.

448 Recording pipettes were pulled from thick-walled filamented borosilicate glass (Sutter  
449 Instruments) using a DMZ Zeitz-Puller (Zeitz) to a tip resistance of 3-8 M $\Omega$  (diameter  $\sim$ 1.25  $\mu$ m),  
450 and filled with internal solution containing (in mM): 130 K-gluconate, 10 HEPES, 0.3 ethylene  
451 glycol-bis( $\beta$ -aminoethyl ether)-N,N,N',N'-tetraacetic acid (EGTA), 3 KCl, 0.23 Na<sub>2</sub>GTP, 6.35  
452 Na<sub>2</sub>Phosphocreatine, 3.4 Mg-ATP, 13.4 Biocytin, and either 25  $\mu$ M Alexa-594 (for optogenetic  
453 experiments), 50  $\mu$ M Cascade Blue dye, or 50  $\mu$ M Alexa-488 (osmolarity between 280 and 295  
454 mOsm titrated with  $\sim$ 4 mM sucrose, pH between 7.2 and 7.3 titrated with  $\sim$ 10 mM KOH). The  
455 liquid junction potential between our internal solution and aCSF 5 was measured to be 9.40 mV  
456  $\pm$  0.59; SD. All electrophysiological values are reported without junction potential correction.

457 In experiments on human tissue and wild-type mice, clusters of up to 8 excitatory neurons  
458 (depth from slice surface  $\geq$  40  $\mu$ m) were selected based on cortical layer and somatic  
459 appearance. In transgenic mice, cells were also targeted based on fluorescent reporter  
460 expression. All cells were confirmed as excitatory post-experiment either by their synaptic  
461 currents onto other recorded neurons (Fig S1A) or by their pyramidal morphology, visualized  
462 using either biocytin (Fig 1A) or fluorescent dye from the pipette (Fig 1B). Cell intrinsic  
463 fluorescence was confirmed post-hoc via manual inspection of image stacks to evaluate signal  
464 overlap of the transgenic fluorescent reporter and the fluorescent dye introduced via pipettes  
465 (Fig 1B). Whole-cell patch clamp electrophysiological recordings were performed at -70 mV to  
466 preferentially measure excitatory inputs. Custom software, Multi-channel Igor Electrophysiology  
467 Suite, written in Igor Pro (WaveMetrics), was used for data acquisition and pipette pressure  
468 regulation. A brief, 10 ms test pulse was used to monitor access and input resistance over the  
469 duration of the recording. Resting membrane potential was maintained within 2 mV using  
470 automated bias current injection during the inter-trial interval. During recordings, cells were  
471 stimulated using brief current injections (1.5 or 3 ms) to drive trains of 12 action potentials  
472 (Figure S1A) at frequencies of 10, 20, 50, or 100 Hz to induce short-term plasticity (STP). A  
473 delay period inserted between the 8th and 9th pulses allowed testing of recovery from STP. In  
474 most recordings this delay period was 250 ms; for 50 Hz stimulation, longer delay periods (500,  
475 1000, 2000, and 4000 ms) were used as well (see Fig 5A). Stimuli were interleaved between  
476 cells such that only one cell was spiking at a time, and no two cells were ever evoked to spike  
477 within 150 ms of each other.

## 478 Data Analysis

479 Postsynaptic recording traces were aligned to the time of the presynaptic spike evoked from the  
480 stimuli described above (Figure S1B). Postsynaptic potentials (PSPs) were identified by manual

481 inspection of individual and averaged pulse-response trials. A classifier (described below) was  
482 later used to highlight possible identification errors, which were then manually corrected.  
483 Connection probabilities within 100  $\mu\text{m}$  intersomatic distance were compared between cell types  
484 using Fisher's exact test of 2x2 contingency tables (connected, unconnected). Bonferroni  
485 method was used to report corrected p values for multiple comparisons among cell types. The  
486 relationship between connectivity and intersomatic distance (measured from 3D cell positions)  
487 was analyzed by binning connections in 40  $\mu\text{m}$  windows and calculating the 95% Jeffreys  
488 Bayesian confidence interval for each bin.

489 Subsets of the 97 mouse and 57 human connections found in this study were analyzed for  
490 strength, kinetics, and STP based on specific quality control criteria (Fig S1C-G, Table 1). EPSP  
491 strength, kinetics, and coefficient of variance (CV) measurements (Fig 1 and 3) were conducted  
492 on the first pulse response of 10, 20, and 50 Hz stimulation trains which were time-aligned to  
493 the presynaptic spike and averaged for each connection. Connections were included for  
494 strength and kinetics analysis according to the analysis flowchart in Fig S1E and F. Briefly, the  
495 postsynaptic cell had an auto bias current less than 800 pA (mean bias current  $-176 \pm 213$  pA),  
496 there was no spontaneous spiking, the stimulus artifact was minimal ( $<30$   $\mu\text{V}$ ), and the PSP was  
497 positive. Individual recording sweeps were included if the baseline potential drift was smaller  
498 than  $\pm 5$  mV from holding ( $-70$  mV) and the mean baseline 10 ms preceding stimulation was  
499 less than 3 standard deviations of the mean baseline across sweeps. In the QC passed data,  
500 strength and kinetics were measured from a double exponential fit that approximates the shape  
501 of the PSP:

$$502 \quad y(t) = A (1 - e^{-(t-t_0)/\tau_r})^2 * e^{-(t-t_0)/\tau_d} \quad (1)$$

503 Best fit parameters were obtained using the Non-Linear Least-Squares Minimization and Curve-  
504 Fitting package for Python (LMFIT; Newville et al., 2014). To improve the quality of fitting, the  
505 root mean square error was weighted (WRMSE) differently throughout the trace. The rising  
506 phase of the PSP was most heavily weighted, the baseline and decay regions were  
507 intermediately weighted, and the region of the presynaptic stimulus, which often contained  
508 crosstalk artifacts was masked. Amplitude was measured as the peak of the PSP fit (Fig S1B).  
509 Kinetics were measured from connections in which the WRMSE of the fit was less than 8.  
510 Latency is reported as the duration from the point of maximum  $dV/dt$  in the presynaptic spike  
511 until the foot of the PSP (Fig S1B), taken from the x-offset in the double exponential fit. Rise  
512 time is reported as the duration from 20% of the peak until 80% of the peak of the PSP (Fig  
513 S1B). Significance of differences in PSP amplitude, latency, and rise time across layers or Cre-  
514 types were assessed with a Kruskal-Wallis test.

515 STP (Fig 5 and 7) was measured from a similar subset of connections that included the quality  
516 control criteria above and also excluded responses smaller than 0.5 mV in amplitude to  
517 minimize the effect of noise on mean response which might impact the model (Fig S1G, Eq. 4  
518 and 5). Connections or individual sweeps that had a baseline holding potential of  $-55$  mV ( $\pm 5$   
519 mV) were reintroduced for this analysis if they met the QC criteria. Normalized PSP amplitudes  
520 (relative to the first pulse) were estimated using an exponential deconvolution ( $\tau=15$  ms;

521 Richardson et al., 2008) to compensate for summation from prior PSPs and to increase signal-  
522 to-noise in measuring PSP amplitudes:

$$523 \quad D(t) = V + \tau \frac{dV}{dt} \quad (2)$$

524 Although the fixed deconvolution time constant of 15 ms may differ significantly from the actual  
525 time constant of each cell, in practice this has little effect on the normalized amplitudes used in  
526 STP measurements (for example, using this time constant to measure amplitudes from a  
527 simulated 100Hz train with a cell time constant of 30 ms only resulted in 3% error in the  
528 measurement of PSP amplitudes relative to the first pulse; data not shown). The peak  
529 amplitudes from the deconvolved traces were used to measure the change in response  
530 magnitude over the course of stimulus trains. We measured the magnitude of short-term  
531 depression or facilitation using the ratio between the first and last (eighth) pulses in an induction  
532 pulse train, whereas recovery from depression or facilitation was measured by the ratio between  
533 the first pulse and the ninth pulse, which followed a recovery delay. Kruskal-Wallis tests were  
534 used to assess significance of STP between multiple layers. A descriptive model was used to  
535 capture features of short-term depression in Rorb, Sim1, and Tlx3 connections (Eq. 4 and 5).

### 536 Automatic synapse detection

537 To aid in the detection of synaptic connections, a support vector machine classifier  
538 (implemented with the "sklearn" python package, Pedregosa et al. 2011) was trained to  
539 discriminate between experiments in which synaptic currents were either visible or not visible to  
540 a human annotator. The classifier required a diverse set of features that were pre-processed  
541 from the raw pulse response recordings. Averaged pulse responses were characterized by  
542 curve fitting (Eq. 1; Fig. 1B) and the fit parameters as well as the normalized RMS error were  
543 provided as features to the classifier. Additionally, individual pulse response recordings were  
544 analyzed by measuring the amplitude and time of the peak of each exponentially deconvolved  
545 response over a 3 ms window, compared to a 10 ms window preceding the stimulus pulse (Fig.  
546 1B, bottom). Although these individual measurements were often noisy (average background  
547 RMS noise  $607 \pm 419 \mu\text{V}$ ), their distribution over hundreds of trials could be compared to similar  
548 distributions measured from background noise (e.g. Fig. 4C). Distributions were compared using  
549 a Kolmogorov-Smirnov test (from the "scipy.stats" Python package) and the p values were used  
550 as input features for the classifier.

551 After training on 1854 manually labeled examples, the classifier was tested against a withheld  
552 set of 2642 examples and achieved an overall accuracy of 95% (56/61 true positive, connected;  
553 2457/2581 true negative, not connected). False positives and negatives were manually  
554 reassessed and frequently found to have been misclassified during the initial manual  
555 annotation; such instances were corrected for in measurements of connectivity.

## 556 Analysis of synapse detection sensitivity

557 To measure the minimum detectable PSP size for each connection probed, artificial PSPs were  
558 added to recordings of background noise taken from the postsynaptic cell. PSPs were  
559 generated using Equation 1 with a foot-to-peak rise time of 2 ms (except where specified in Fig  
560 3D). PSP latencies were selected from a gaussian distribution centered at 2 ms with a 200  $\mu$ s  
561 standard deviation. PSP amplitudes were generated by the product of two random variables:  
562 one binomially distributed ( $p=0.2$ ,  $n=24$ ) to mimic stochastic vesicle release, and the other  
563 normally distributed (mean=1, SD=0.3) to account for differences in vesicle size and receptor  
564 efficacy. PSPs were then scaled uniformly to achieve a specific mean amplitude. The resulting  
565 simulated responses were qualitatively similar to typical synaptic responses encountered in our  
566 dataset, although they lacked the synapse-to-synapse variability in CV, due to the selection of  
567 fixed distribution parameters listed above.

568 For each connection probed, the number of simulated PSPs generated was the same as the  
569 number of presynaptic spikes elicited during the experiment. These PSPs were then fed through  
570 the same preprocessing and classification system that was used to detect synaptic connections  
571 in real data, and the classification probability was calculated from the classifier (using  
572 `sklearn.svm.SVC.predict_proba`). This process was repeated 8 times (with PSPs generated  
573 randomly each time) and the average classification probability was recorded. This yields an  
574 estimate of whether a synaptic connection would be detected or overlooked, given the  
575 combination of sample count, background noise characteristics, and PSP strength and kinetics.

576 By repeating this process for several different values of mean PSP amplitude, we could identify,  
577 for each putative connection probed, a plausible minimum detectable PSP amplitude. This  
578 minimum detectable amplitude was defined as the PSP amplitude at which the classifier would  
579 detect the synapse in 50% of trials (interpolated from adjacent amplitudes).

## 580 PSP amplitude run-down over duration of experiment

581 The amplitude of the PSPs initiated by the first pulse of the stimulus trains was characterized  
582 over time for the same subset of connections described for the strength and kinetics analysis. In  
583 order to discount variations in the measurements of individual first pulses, the run-down was  
584 characterized via a linear regression of PSP amplitude versus time. Here, the total run-down is  
585 reported as the percentage decrease in amplitude of a PSP at the beginning and end of an  
586 experiment (average duration was  $24.4 \pm 10.8$  minutes) specified by the linear regression, i.e.  
587 percent run-down,

$$588 \quad \text{Percent Decay} = \frac{PSP_{final} - PSP_{initial}}{PSP_{initial}} * 100 \quad (3)$$

589 All synapses where the beginning and ending PSP amplitude straddled zero, which can happen  
590 for the weaker synapses, were excluded from analysis as they produce aberrant percentage  
591 values. On median, the following overall run-downs were observed: layer 2/3 to layer 2/3  
592 connections 11%, Rorb to Rorb 31%, Sim1 to Sim1 22%, Tlx3 to Tlx3 16%.

## 593 Theoretical Synaptic Modelling

594 Synaptic depression was modelled via depletion of vesicles (Hennig, 2013; Mongillo et al.,  
595 2008; Richardson et al., 2005),

$$596 \quad \frac{dn}{dt} = \frac{1-n}{\tau_r} - P_0 n \delta(t - t_k) \quad (4)$$

597 where  $n$  is the fraction of available vesicles,  $P_0$  is the release probability,  $t_k$  is the time of  
598 presynaptic spike and  $\tau_r$  is the time constant for vesicle replenishment. The speed of  
599 replenishment can vary over time depending on the history of presynaptic spikes, which can be  
600 captured by time constant  $\tau_r$  evolving according to Eq. 5 (Fuhrmann et al., 2002; Hennig, 2013),

601

$$602 \quad \frac{d\tau_r}{dt} = \frac{\tilde{\tau}_{r0} - \tau_r}{\tau_{FDR}} - a_{FDR} \tau_r \delta(t - t_k) \quad (5)$$

603 where  $\tau_{FDR}$  is the time constant of use-dependent replenishment,  $a_{FDR}$  represents the amount  
604 of updates elicited by a presynaptic spike and  $\tilde{\tau}_{r0}$  is the baseline time constant.

605 For Rorb, Sim1, and Tlx3 synapses, we optimized the parameters ( $P_0$ ,  $\tilde{\tau}_{r0}$ ,  $\tau_{FDR}$  and  $a_{FDR}$ ) to  
606 account for time courses of PSPs. Specifically, PSPs were averaged over all available synapses  
607 depending on stimulation frequencies and delays between 8<sup>th</sup> and 9<sup>th</sup> presynaptic pulses and  
608 fitted to the model. We used LMFIT (Newville et al., 2014) to perform non-linear least-square  
609 minimization.

610 Paired Z-scores for  $P_0$  and  $\tau_{r0}$  were calculated from the standard error returned during  
611 parameter optimization according to Eq 6.,

$$612 \quad \text{Z-score} = \frac{|X_1 - X_2|}{\sqrt{SE_1^2 + SE_2^2}} \quad (6)$$

613 Where  $X_1$  and  $X_2$  are  $P_0$  or  $\tau_{r0}$  for 2 groups and their associated standard error.

## 614 Histology and Morphology

615 After completing electrophysiological recordings, slices were transferred from the recording  
616 chamber and fixed in solution containing 4% PFA and 2.5% glutaraldehyde for 2 days (>40  
617 hours) at 4°C. After fixation, slices were transferred and washed in phosphate buffer saline  
618 (PBS) solution for 1-7 days.

619 Sections were processed using 3,3'-diaminobenzidine (DAB) peroxidase substrate kit to identify  
620 recorded neurons filled with biocytin. Free floating sections were first incubated with 5  $\mu$ M 4',6-  
621 diamidino-2-phenylindole (DAPI) in PBS for 15 minutes at room temperature and then triple  
622 washed in PBS (3 x 10 minutes). Sections were transferred to a 1% H2O2 (in PBS) for 30



623 minutes and then triple washed in PBS. A DAB substrate kit (VectorLabs) was used to stain for  
624 neurons filled with biocytin. Sections were mounted on gelatin-coated slides and coverslipped  
625 with Aqua-Poly/Mount (Polysciences).

626 Slides were imaged on an AxioImager Z2 microscope (Zeiss) equipped with an AxioCam 506  
627 camera (Zeiss) and acquired via the Zeiss Efficient Navigation software. Tiled mosaic images of  
628 whole slices were acquired via automated scanning and stitching of several 20X images to  
629 generate both brightfield and DAPI images of the entire slice.

## 630 Two photon optogenetic experiments

631 Connectivity mapping experiments were performed on a two-photon laser scanning microscope  
632 (Bruker Corp) with a tunable pulsed Ti:Sapphire laser (Chameleon Ultra, Coherent) for imaging,  
633 and a fixed wavelength (1060 nm) pulsed laser (Fidelity Femtosecond, Coherent) for  
634 stimulation. A 63x, 1.0 NA water immersion objective (Zeiss) was used for all experiments. Two-  
635 photon images were acquired with PrairieView software (Bruker Corp), and stimulation targets  
636 were manually placed on these reference images to target ReaChR-positive cells.

637 Photoactivation stimuli were triggered by a TTL pulse generated within MIES acquisition  
638 software. The voltage output controlling the photoactivation Pockels cell was recorded within  
639 MIES for post-hoc alignment of physiological recordings with the timing of photoactivation. To  
640 characterize the effectiveness and specificity of stimulation parameters, we made loose seal  
641 recordings on to EYFP/ReaChR-labelled neurons (Figure S2A). For all data presented here, the  
642 photostimulation pattern consisted of a spiral 5  $\mu\text{m}$  in diameter with 5 revolutions traced over a  
643 25 ms duration. We first determined the minimum light power necessary to evoke reliable firing  
644 of action potentials. This minimum power varied across cells from 2.6 -20.3 mW (Figure S2B). A  
645 photo-stimulus of 18 mW intensity was sufficient to evoke spiking in 92% of cells tested (12/13  
646 cells). The average latency of firing at this power was  $12.9 \pm 6.1$  ms and the associated jitter  
647 was  $0.98 \pm 0.58$  ms (Figure S2C,D).

648 Within the same experiments, we characterized the spatial specificity of these stimulation  
649 parameters. First, to determine the probability of off-target photoactivation of cells within the  
650 same focal plane, we delivered stimuli in a radial grid pattern containing 7 spokes with stimuli  
651 spaced 10, 20 and 30  $\mu\text{m}$  away from the center of the recorded cell (Figure S2E). Spike  
652 probability fell to 0.5 at a lateral distance of 12.0  $\mu\text{m}$ . Finally, we determined the axial resolution  
653 of our photoactivation paradigm by offsetting the focus of the objective relative to the recorded  
654 cell. Consistent with previous studies, (Packer et al., 2012; Prakash et al., 2012) axial resolution  
655 was inferior compared to lateral resolution (spike probability = 0.5 at 26.7  $\mu\text{m}$ ) but was still near  
656 cellular resolution (Figure S2F).

657 For two photon mapping experiments, 1-2 neurons were patched and membrane potential was  
658 maintained near -70 mV with auto bias current injection. Neurons were filled with 50  $\mu\text{M}$  Alexa-  
659 594 to visualize cell morphology (Figure S3A). The orientation of the apical dendrite was utilized  
660 to align photostimulation sites across experiments in downstream analyses. Each putative  
661 presynaptic neuron was stimulated 10-20 times, with the parameters described above.  
662 Photostimulation was performed in 'rounds' during which EYFP-labelled neurons within a single

663 field of view were sequentially targeted (3-12 neurons/round). Stimulation protocols were  
664 constrained such that the inter-stimulus interval between neurons was  $\geq 2$  s and the inter-  
665 stimulus interval for a given neuron was  $\geq 10$  s.

666 Photostimulus responses were scored as connection, no connection or as containing a direct  
667 stimulation artifact by manual annotation. To assist in these user-generated calls, we  
668 incorporated a signal-to-noise measure for our optogenetic mapping data. Current clamp traces  
669 were low pass filtered at 1 kHz and baseline subtracted. The voltage-deconvolution technique  
670 (Eq. 2) was then applied. The value of  $\tau$  was set between 10-40 ms. Deconvolved traces were  
671 high pass filtered at 30 Hz, and peaks larger than 3 standard deviations above pre-stimulus  
672 baseline were used for further analysis (Fig 4 S3B,C). We then measured the number of peaks  
673 in both 'signal' and 'noise' regions. The 'signal' region was a 100 ms window 5-105 ms after the  
674 onset of the photostimulus, and the 'noise' region was a 100 ms window 145-45 ms before the  
675 stimulus onset. To compensate for jitter known to be present in two-photon mediated  
676 stimulation, we determined a 10 ms subset within each 100 ms window that gave the maximum  
677 number of unique trials containing threshold-crossing events. The median of the peak within this  
678 10 ms window was found across all trials in both 'signal' and 'noise' regions, and the mean of a  
679 25 ms window preceding both regions was subtracted to produce our final signal and noise  
680 values.

681 We plotted the signal against the noise for all stimulus locations (Fig 4 S3D), and found that  
682 most points with a high signal-to-noise ratio contained either a synaptic response or an artifact  
683 produced by direct stimulation of the recorded (opsin-expressing) cell. 93% (13/14) manually  
684 identified connections had a signal to noise ratio  $> 1.5$  (Fig 4 S3E). By contrast, the same was  
685 true of only 1.7% (24/1416) of cells scored as 'no connection'. Therefore, our signal to noise  
686 analyses highlight quantitatively distinct features of our connection calls. The presence of direct  
687 stimulation artifacts prevents us from unambiguously identifying synaptic connections between  
688 nearby neurons. Therefore, when estimating connection probability by two-photon optogenetics,  
689 we did not include putative presynaptic cells within 50  $\mu\text{m}$  of the recorded neuron where the  
690 direct stimulation artifact was largest (Fig 4F).

## 691 Acknowledgments

692 The authors thank the Allen Institute founder, Paul G. Allen, for his vision, encouragement and  
693 support. Thank you to the Allen Institute for Brain Science Tissue Processing, Histology,  
694 Imaging, and Morphology and 3D reconstruction teams for preparing and processing mouse  
695 tissue. We further thank the Tissue Procurement, Tissue Processing, and Facilities teams for  
696 help in coordinating the logistics of human surgical tissue collection, transport, and processing.  
697 We are also grateful to our collaborators at the local hospital sites, including Tracie Granger,  
698 Caryl Tongco, Matt Ormond, Jae-Guen Yoon, Nathan Hansen, Niki Ellington, Rachel Iverson  
699 (Swedish Medical Center), Carolyn Bea, Gina DeNoble and Allison Beller (Harborview Medical  
700 Center). We thank Dirk C. Keene at Harborview/UW for consultation and support. This work was

701 supported by the Allen Institute for Brain Science, National Institutes of Health grant  
702 U01MH105982 to H.Z., and the Howard Hughes Medical Institute grant to GJM.

## 703 Competing Interests

704 The authors declare that there are no conflicts of interest.

## 705 References

706 Abbott, Varela, Sen, Nelson (1997) Synaptic depression and cortical gain control. *Science*  
707 275:221–224.

708  
709 Barth, Burkhalter, Callaway, Connors, Cauli, DeFelipe, Feldmeyer, Freund, Kawaguchi,  
710 Kisvarday, Kubota, McBain, Oberlaender, Rossier, Rudy, Staiger, Somogyi, Tamas, Yuste  
711 (2016) Comment on “Principles of connectivity among morphologically defined cell types in adult  
712 neocortex.” *Science* 353:1108–1108.

713  
714 Biane, Takashima, Scanziani, Conner, Tuszynski (2016) Thalamocortical projections exhibit  
715 plasticity onto behaviorally-relevant neurons during adult motor learning. *Neuron* 89(6):1173-  
716 1179.

717  
718 Binzegger, Douglas, Martin (2004) A quantitative map of the circuit of cat primary visual cortex.  
719 *The Journal of Neuroscience* 24:8441–8453.

720  
721 Bopp, Costa, Kampa, KAC M, Roth. 2014. Pyramidal Cells Make Specific Connections onto  
722 Smooth (GABAergic) Neurons in Mouse Visual Cortex. *PLoS Biology* 12:e1001932.

723  
724 Borst (2010) The low synaptic release probability in vivo. *Trends in Neurosciences* 33:259–266.

725  
726 Braitenberg, Schüz (1998) *Cortex: statistics and geometry of neuronal connectivity*, 2nd  
727 Edition. Berlin: Springer.

728  
729 Brunel (2016) Is cortical connectivity optimized for storing information? *Nature Neuroscience*  
730 19:749–755.

731  
732 Campagnola, Kratz, Manis. 2014. ACQ4: an open-source software platform for data acquisition  
733 and analysis in neurophysiology research. *Frontiers in Neuroinformatics* 8:3.

734  
735 Camperi, Wang (1998) A model of visuospatial working memory in prefrontal cortex: recurrent  
736 network and cellular bistability. *Journal of Computational Neuroscience* 5(4):383-405.

737  
738 Cossell, Iacaruso, Muir, Houlton, Sader, Ko, Hofer, Mrsic-Flogel (2015) Functional organization  
739 of excitatory synaptic strength in primary visual cortex. *Nature* 518:399–403.

740

741 Daigle, Madisen, Hage, Valley, Knoblich, Larsen, Takeno, Huang, Gu, Larsen, Mills, Bosma-  
742 Moody, Siverts, Walker, Graybuck, Yao, Fong, Garren, Lenz, Chavarha, Pendergraft,  
743 Harrington, Hirokawa, Harris, McGraw, Ollerenshaw, Smith, Baker, Ting, Sunkin, Lecoq, Lin,  
744 Boyden, Murphy, Costa, Waters, Li, Tasic, Zeng (2017) A suite of transgenic driver and reporter  
745 mouse lines with enhanced brain cell type targeting and functionality. *bioRxiv*:224881.  
746  
747 Fuhrmann, Segev, Markram, Tsodyks (2002) Coding of temporal information by activity-  
748 dependent synapses. *Journal of Neurophysiology* 87:140–148.  
749  
750 Galarreta, Hestrin (1998) Frequency-dependent synaptic depression and the balance of  
751 excitation and inhibition in the neocortex. *Nature Neuroscience* 1:587–594.  
752  
753 Hennig (2013) Theoretical models of synaptic short term plasticity. *Frontiers in Computational*  
754 *Neuroscience* 7:45.  
755  
756 Holmgren, Harkany, Svennenfors, Zilberter (2003) Pyramidal cell communication within local  
757 networks in layer 2/3 of rat neocortex. *The Journal of Physiology* 551:139–153.  
758  
759 Isaac, Nicoll, Malenka. 1995. Evidence for silent synapses: Implications for the expression of  
760 LTP. *Neuron* 15:427–434.  
761  
762 Jiang, Shen, Cadwell, Berens, Sinz, Ecker, Patel, Tolias (2015) Principles of connectivity among  
763 morphologically defined cell types in adult neocortex. *Science* 350:aac9462.  
764  
765 Jiang, Shen, Sinz, Reimer, Cadwell, Berens, Ecker, Patel, Denfield, Froudarakis, Li, Walker,  
766 Tolias (2016) Response to Comment on “Principles of connectivity among morphologically  
767 defined cell types in adult neocortex.” *Science* 353:1108–1108.  
768  
769 Jouhanneau, Kremkow, Dornn, Poulet (2015) In vivo monosynaptic excitatory transmission  
770 between layer 2 cortical pyramidal neurons. *Cell Reports* 13:2098–2106.  
771  
772 Kim, Juavinett, Kyubwa, Jacobs, Callaway (2015) Three types of cortical layer 5 neurons that  
773 differ in brain-wide connectivity and function. *Neuron* 88(6):1253-1267.  
774  
775 Kisvárdy, KAC M, Freund, Maglóczy, Whitteridge, Somogyi. 1986. Synaptic targets of HRP-  
776 filled layer III pyramidal cells in the cat striate cortex. *Experimental Brain Research* 64:541–552.  
777  
778 Lee, Bonin, Reed, Graham, Hood, Glattfelder, Reid (2016) Anatomy and function of an  
779 excitatory network in the visual cortex. *Nature* 532(7599):370-374.  
780  
781 Lefort, Tomm, Sarria, Petersen (2009) The excitatory neuronal network of the C2 barrel column  
782 in mouse primary somatosensory cortex. *Neuron* 61:301–316.  
783

784 Lefort, Petersen (2017) Layer-dependent short-term synaptic plasticity between excitatory  
785 neurons in the C2 barrel column of mouse primary somatosensory cortex. *Cerebral Cortex*  
786 27:3869-3878.  
787  
788 Levy, Reyes (2012) Spatial profile of excitatory and inhibitory synaptic connectivity in mouse  
789 primary auditory cortex. *The Journal of Neuroscience* 32:5609–5619.  
790  
791 Lin, Knutsen, Muller, Kleinfeld, Tsien (2013) ReaChR: a red-shifted variant of channelrhodopsin  
792 enables deep transcranial optogenetic excitation. *Nature Neuroscience* 16:1499–1508.  
793  
794 Markram (1997) A network of tufted layer 5 pyramidal neurons. *Cerebral Cortex* 7:523–533.  
795  
796 Markram et al. (2015) Reconstruction and simulation of neocortical microcircuitry. *Cell* 163:456–  
797 492.  
798  
799 Mason, Nicoll, Stratford (1991) Synaptic transmission between individual pyramidal neurons of  
800 the rat visual cortex in vitro. *The Journal of Neuroscience* 11:72–84.  
801  
802 McGuire, Gilbert, Rivlin, Wiesel. 1991. Targets of horizontal connections in macaque primary  
803 visual cortex. *Journal of Comparative Neurology* 305:370–392.  
804  
805 Molnár, Oláh, Komlósi, Füle, Szabadics, Varga, Barzó, Tamás (2008) Complex events initiated  
806 by individual spikes in the human cerebral cortex. *PLoS Biology* 6:e222.  
807  
808 Mongillo, Barak, Tsodyks (2008) Synaptic theory of working memory. *Science* 319:1543–1546.  
809  
810 Morishima, Morita, Kubota, Kawaguchi (2011) Highly differentiated projection-specific cortical  
811 subnetworks. *The Journal of Neuroscience* 31:10380–10391.  
812  
813 Newville, Stensitzki, Allen, Ingargiola (2014) LMFIT: Non-linear least-square minimization and  
814 curve-fitting for Python.  
815  
816 Olshausen, Field (1996) Emergence of simple-cell receptive field properties by learning a  
817 sparse code for natural images. *Nature* 381:607-609.  
818  
819 Packer, Peterka, Hirtz, Prakash, Deisseroth, Yuste (2012) Two-photon optogenetics of dendritic  
820 spines and neural circuits. *Nature Methods* 9:nmeth.2249.  
821  
822 Pala, Petersen (2015) In vivo measurement of cell-type-specific synaptic connectivity and  
823 synaptic transmission in layer 2/3 mouse barrel cortex. *Neuron* 85:68–75.  
824 Pedregosa, Varoquaux, Gramfort, Michel, Thirion, Grisel, Blondel, Louppe, Prettenhofer, Weiss,  
825 Dubourg, Vanderplas, Passos, Cournapeau, Brucher, Perrot, É D. 2012. Scikit-learn: Machine  
826 Learning in Python.  
827

- 828 Perin, Berger, Markram (2011) A synaptic organizing principle for cortical neuronal groups.  
829 Proceedings of the National Academy of Sciences 108:5419–5424.  
830
- 831 Pernice, RAD S (2018) Interpretation of correlated neural variability from models of feed-forward  
832 and recurrent circuits. PLoS Computational Biology 14:e1005979.  
833
- 834 Peters (1979) Thalamic input to the cerebral cortex. Trends in Neurosciences 2:183–185.  
835
- 836 Prakash, Yizhar, Grewe, Ramakrishnan, Wang, Goshen, Packer, Peterka, Yuste, Schnitzer,  
837 Deisseroth (2012) Two-photon optogenetic toolbox for fast inhibition, excitation and bistable  
838 modulation. Nature Methods 9:nmeth.2215.  
839
- 840 Reyes, Lujan, Rozov, Burnashev, Somogyi, Sakmann (1998) Target-cell-specific facilitation and  
841 depression in neocortical circuits. Nature Neuroscience 1:279–285.  
842
- 843 Reyes, Sakmann (1999) Developmental switch in the short-term modification of unitary EPSPs  
844 evoked in layer 2/3 and layer 5 pyramidal neurons of rat neocortex. The Journal of  
845 Neuroscience 19:3827–3835.  
846
- 847 Richardson, Melamed, Silberberg, Gerstner, and Markram (2005) Short-term synaptic plasticity  
848 orchestrates the response of pyramidal cells and interneurons to population bursts. Journal of  
849 Computational Neuroscience 18:323–331.  
850
- 851 Richardson, Silberberg (2008) Measurement and analysis of postsynaptic potentials using a  
852 novel voltage-deconvolution method. Journal of Neurophysiology 99:1020-1031.  
853
- 854 Sejnowski, Koch, Churchland (1988) Computational neuroscience. Science 241:1299–1306.  
855
- 856 Sjostrom, Turrigiano, Nelson (2001) Rate, timing, and cooperativity jointly determine cortical  
857 synaptic plasticity. Neuron 32(6):1149-1164.  
858
- 859 Song, Sjöström, Reigl, Nelson, Chklovskii (2005) Highly nonrandom features of synaptic  
860 connectivity in local cortical circuits. PLoS Biology 3:e68.  
861
- 862 Stepanyants, Martinez, Ferecskó, Kisvárdy (2009) The fractions of short- and long-range  
863 connections in the visual cortex. Proceedings of the National Academy of Sciences 106:3555–  
864 3560.  
865
- 866 Tasic et al. (2016) Adult mouse cortical cell taxonomy revealed by single cell transcriptomics.  
867 Nature Neuroscience 19:335–346.  
868
- 869 Ting, Daigle, Chen, Feng (2014) Methods in Molecular Biology. Methods in molecular biology  
870 (Clifton, NJ) 1183:221–242.  
871

872 Urban-Ciecko, Fanselow, Barth (2015) Neocortical somatostatin neurons reversible silence  
873 excitatory transmission via GABA<sub>B</sub> receptors. *Current Biology* 25(6):722-731  
874  
875 van Pelt, van Ooyen (2013) Estimating neuronal connectivity from axonal and dendritic density  
876 fields. *Frontiers in Computational Neuroscience* 7:160.  
877  
878 Wang, Markram, Goodman, Berger, Ma, Goldman-Rakic (2006) Heterogeneity in the pyramidal  
879 network of the medial prefrontal cortex. *Nature Neuroscience* 9:534–542.  
880  
881 Zeng, Horie, Madisen, Pavlova, Gragerova, Rohde, Schimpf, Liang, Ojala, Kramer, Roth,  
882 Slobodskaya, Dolka, Southon, Tessarollo, Bornfeldt, Gragerov, Pavlakis, Gaitanaris (2008) An  
883 inducible and reversible mouse genetic rescue system. *PLoS Genetics* 4:e1000069.  
884  
885 Zhao, Ting, Atallah, Qiu, Tan, Gloss, Augustine, Deisseroth, Luo, Graybiel, Feng (2011) Cell  
886 type-specific channelrhodopsin-2 transgenic mice for optogenetic dissection of neural circuitry  
887 function. *Nature Methods* 8:nmeth.1668.

888 Supplement

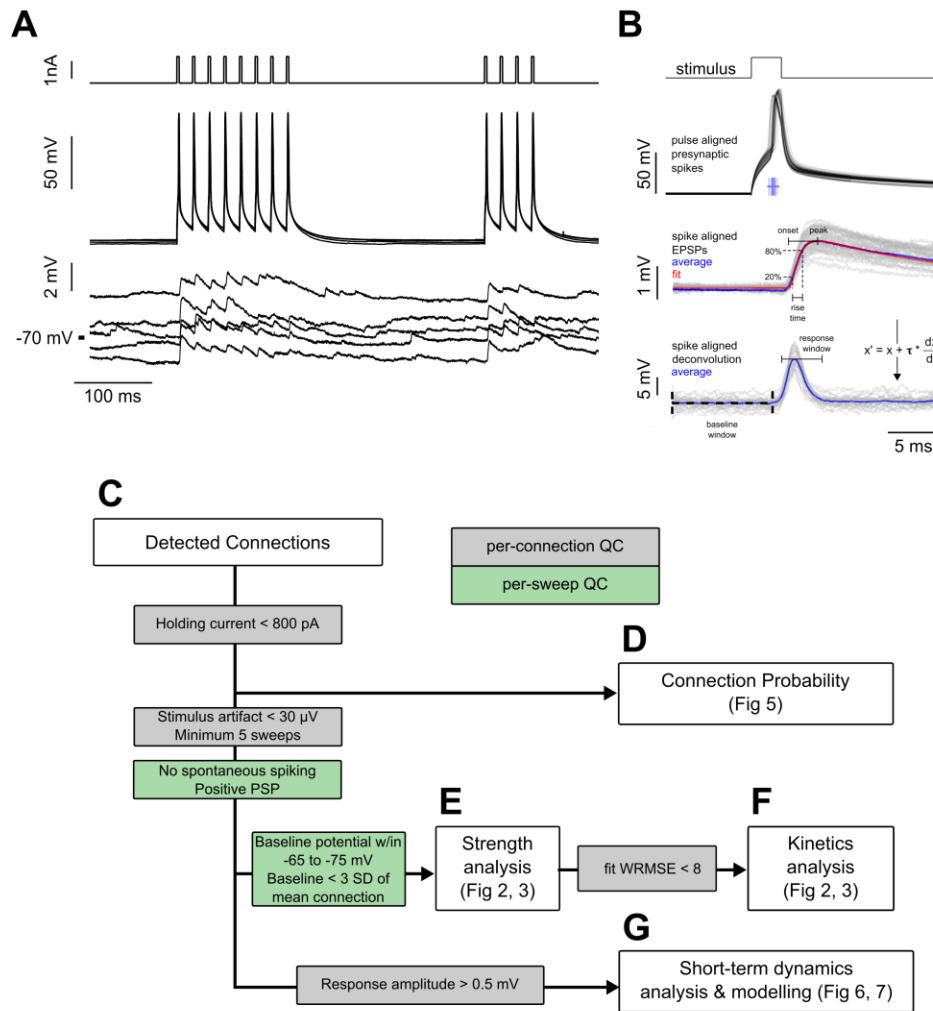


**Figure S1** Experiment methodology and analysis workflow. **A.** Example connected pair showing the stimulation pulses (top) and action potentials (middle) in the presynaptic cell; monosynaptically evoked EPSPs (bottom) in the postsynaptic cell. Traces represent every fifth sweep from the 50 Hz protocol used to measure recovery from STP at a delay of 250 ms. **B.** Following repeated stimulation, the response to the first spike in each train of current pulses was used for EPSP feature analysis. Spikes are shown aligned to the pulse time to illustrate jitter in spike timing. Spike time was defined as the region of maximum  $dV/dt$  in the spike trace, as shown in the raster plot corresponding to spike timing of individual spikes. Below, EPSPs are aligned to the spike time prior to fitting the average EPSP (see Equation 1; individual sweeps in grey, average response in blue, fit shown in red). The rise time was calculated as the interval between 20% and 80% of the peak amplitude of the fit. Spike-aligned EPSPs were deconvolved (see Equation 2, shown in figure), and the peak amplitudes of the deconvolved traces were used to measure changes in response amplitude of the course of a spike train. Responses were corrected to the baseline by subtracting the mode of the region between 10 ms and 50  $\mu$ s prior to stimulus onset (baseline window). Responses were measured as the peak response during a 4 ms window beginning 1 ms after the spike time (response window shown is aligned to mean spike time). **C-G.** Subsets of total connectivity data were used in subsequent analysis. Flowchart shows sweep (green) and connection (grey) level inclusion criteria for data included in each figure. See Table 1 for total number of cells in each criterion.



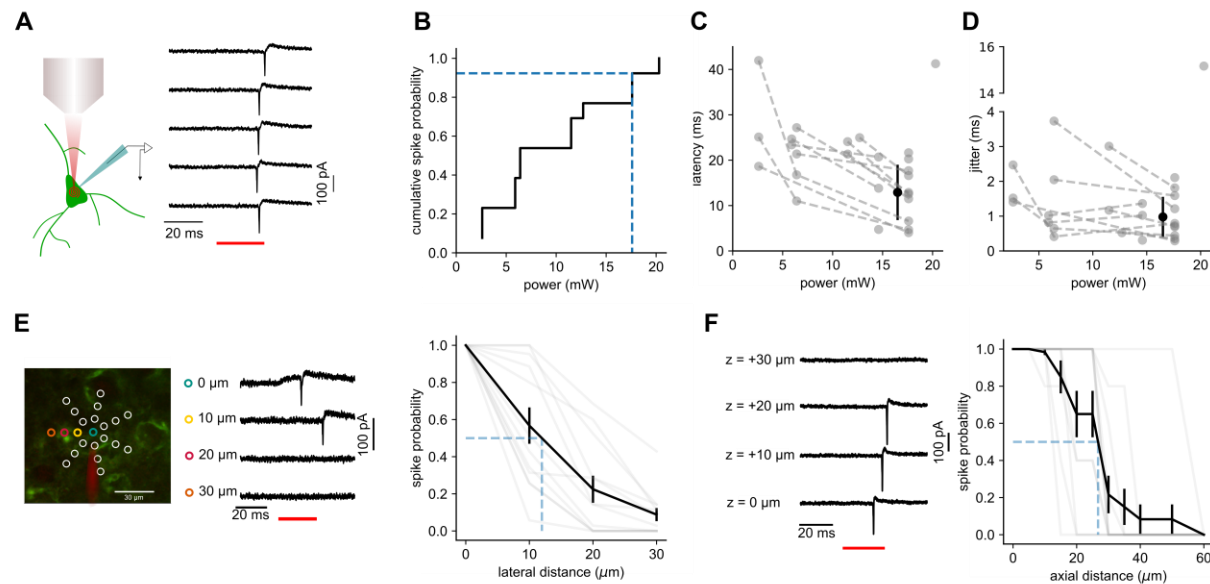


**Figure S2** Characterization of two-photon photostimulation. **A.** Cartoon illustrating loose-seal recording configuration utilized to test photostimulation parameters. Example recording of repeated photostimulation of a ReaChR-positive cell. **B.** Cumulative probability plot of minimum power necessary to reliably evoke action potentials for 13 cells. Blue dashed lines indicate light power utilized in mapping experiments and the fraction of cells reliably activated. **C.** Average latency of light-evoked action potentials plotted against photostimulation intensity for individual neurons (grey dashed lines). Filled black circle and error bars represent the mean and standard deviation of latency measured across all cells at a power used for mapping. **D.** Average jitter of light-evoked action potentials plotted against photostimulation intensity. Data from individual cells and population average plotted as in panel C. **E. Left:** Example experiment illustrating the radial grid pattern used to measure the lateral resolution of photostimulation and example traces recorded during the photostimulation at indicated locations. **Right:** Probability of generating light-evoked action potentials plotted against lateral distance from the center of the cell. **F. Left:** example of responses resulting from photostimulation at indicated axial offsets. **Right:** Probability of generating light-evoked action potentials plotted against axial distance from the center of the cell.

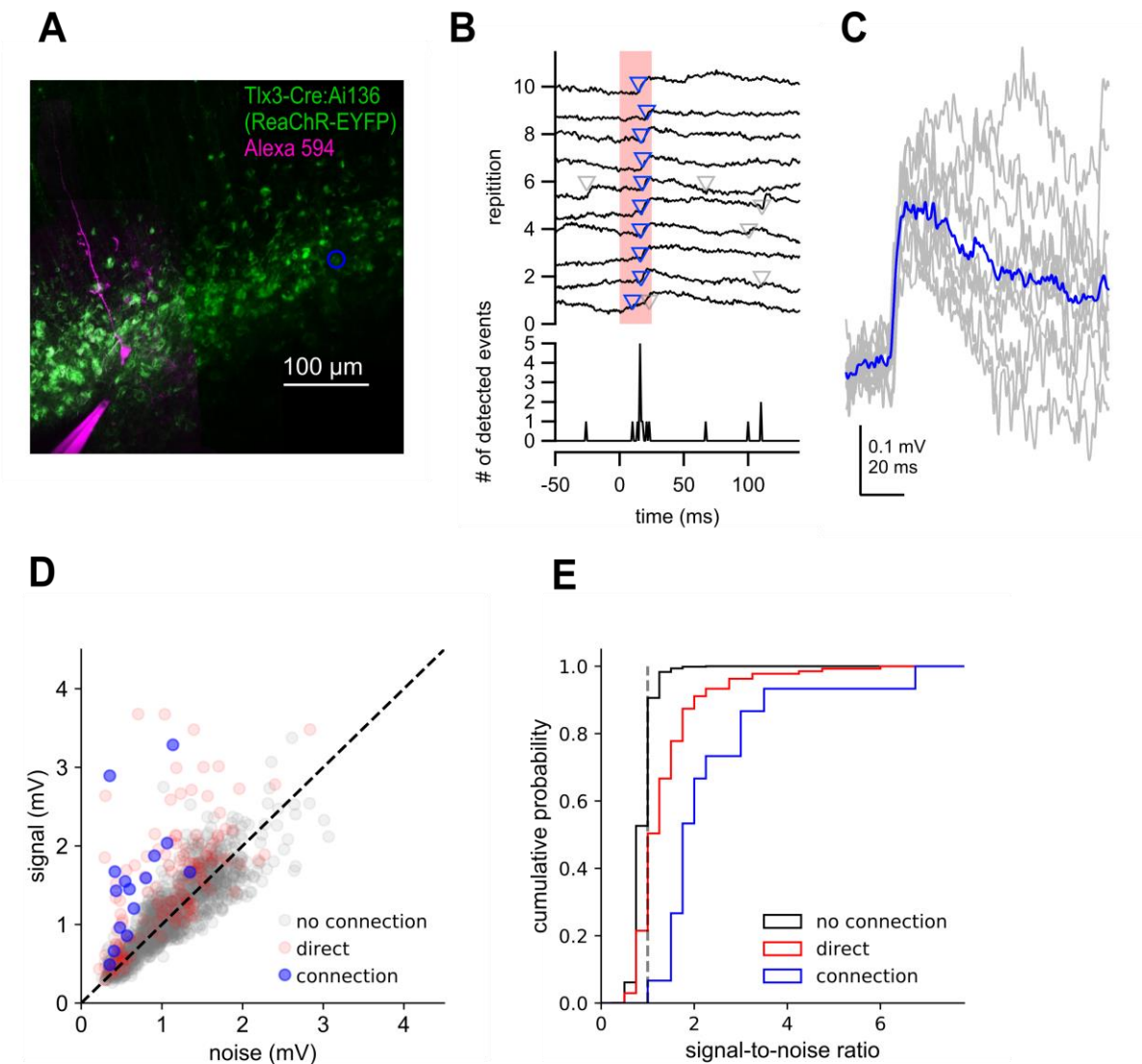


**Figure S3** Two-photon optogenetic mapping details. **A.** Maximum intensity projection of Tlx3-Cre: Ai136 slice and a recorded neuron. Blue circle denotes location of stimulated presynaptic neuron. **B.** *Top:* Electrophysiological recording of postsynaptic response to 10 photostimulations of the presynaptic neuron in panel A. Timing of photostimulation indicated by pink shading. Synaptic events detected by exponential deconvolution are indicated by inverted triangles. Events used to produce average synaptic response are shown in blue. *Bottom:* Peri-stimulus event histogram. **C.** Individual events aligned by the timing of event detection (grey) and average EPSP (blue). **D.** Signal versus noise plot for all optogenetically-probed presynaptic neurons. **E.** Cumulative probability plot of signal-to-noise ratios for stimulus trials scored as no connection, connection, or containing a direct stimulation artifact. Dashed grey line indicates signal-to-noise ratio = 1.